Slightly deformable Darcy drop in linear flows

Y.-N. Young, Yoichiro Mori, and Michael J. Miksis

Phys. Rev. Fluids **4**, 063601 — Published 5 June 2019

DOI: 10.1103/PhysRevFluids.4.063601

A Slightly Deformable Darcy Drop in Linear Flows

Y.-N. Young[1], Yoichiro Mori[2] and Michael J. Miksis[3]
[1]*Department of Mathematical Sciences,*
New Jersey Institute of Technology, Newark, New Jersey, 07102, USA
[2]*Department of Mathematics, University of Minnesota,*
Minneapolis, Minnesota, 55455, USA
[3]*Department of Engineering Sciences and Applied Mathematics,*
Northwestern University, Evanston, Illinois, 60208, USA
(Dated: May 17, 2019)

Abstract

A two-phase flow model is developed to study the small-deformation of a poroelastic drop under linear flows. Inside the drop a deformable porous network characterized by an elastic modulus is fully immersed in a viscous fluid. When the viscous dissipation of the interior fluid phase is negligible (compared to the friction between the fluid and the skeleton), the two-phase flow is reduced to a poroelastic Darcy flow with a deformable porous network. At the interface between the poroelastic drop and the exterior viscous Stokes flow, a novel set of boundary conditions are derived by the free energy dissipation principle. Both interfacial slip and permeability are taken into account and the permeating flow induces dissipation that depends on the elastic stress of the interior solid. Assuming that the porous network has a large elastic modulus a small-deformation analysis is conducted. A steady equilibrium is computed for two linear applied flows: a uniaxial extensional flow and a planar shear flow. By exploring the interfacial slip, permeability and network elasticity various flow patterns are found at equilibrium of these slightly deformed poroelastic drops. Linear dynamics of the small-amplitude deviation of the poroelastic drop from the spherical shape is governed by a nonlinear eigenvalue problem, and the eigenvalues are determined.

PACS numbers: Valid PACS appear here

I. INTRODUCTION

Flow in porous media is of significant relevance to many research areas, ranging from turbulent transport through porous media in geophysics, filtration in hydrology, to cell and tissue mechanics in bio-mechanical engineering. A great deal of effort has been devoted to the modeling of pressure-driven fluid flow, thermal convection and propagation of sound waves in porous media, and the fluid pressure in water-filled connective tissues such as the cornea. Depending on the specific applications, the porous structures may be treated either as rigid and non-deformable (as in hydrology of filtration), or they may deform as their dynamics is coupled to the fluid flow around them (as in tissue mechanics). Here we focus on the latter case.

In many applications, the porous flow is in the Stokes regime where the inertia is negligible. For a Stokes flow going through a non-deformable porous medium, homogenization analysis shows that on macroscopic scales (much larger than the average pore size) such a porous flow is simplified to a Darcy's flow[1]. The viscous stress in the fluid is negligible after homogenization, and the dominant force balance is between the pressure gradient and a frictional force between the viscous fluid and the rigid porous frame. In solid mechanics this frictional force is derived from a dissipative potential assumed for the solid-fluid interaction (see Carcione [2] and references therein). A similar homogenization analysis also predicts a Brinkmann flow (viscous stress is comparable with both pressure gradient and the frictional force) when the solid volume fraction is less than 5% (porosity is greater than 95%).

When the porous structure (skeleton phase) is deformable and the pore space is completely filled with a viscous fluid, the mechanics of the skeleton is inevitably intertwined with the hydrodynamics of the viscous fluid. For example, the pore space increases when fluid is injected to expand the skeleton while compressing the skeleton will drive fluid out as the pore space shrinks. In the presence of an external pressure jump, MacMinn *et al.* focused on the coupling between the interior fluid flow and the deformation of a nonlinear elastic porous structure. They reported both small and large deformations of the poro-elastic structures using various elastic models. In particular they studied the one-dimensional dynamic evolution from an initial configuration towards a steady equilibrium.

While in geophysics the pressure-driven Darcy flow inside a poroelastic skeleton is of great relevance, in biophysics the poroelastic flows inside the cell are either driven by or coupled with the exterior viscous fluid flow [3–6]. Two-phase flow models have been derived to capture the coupled dynamics between a poroelastic flow and the external viscous fluid flow [7–10]. In these models, the viscous dissipation in the fluid phase may be comparable to the pressure gradient, and this coupling can be further complicated by ion transport in the porous medium flow [8].

Cogan and Keener developed a two-phase flow model for the cellular cytosol dominated by viscous dissipation of the deformable skeleton (that depends on the rate of strain) and independent of the elastic energy (that depends on the strain) [7]. A similar two-phase flow model is constructed for the cellular cytosolic flow [9, 10], where the immersed boundary method is used to calculate the extra stress in the skeleton and no explicit boundary conditions for the velocity field are provided. Mori *et al.* constructed a two-phase flow model to

incorporate the electrochemical mechanics of a polyelectrolytic fluids such as the cytosol [8]. Focusing on the variational analysis of the governing equations in the mean-field framework, their dynamical model consists of an interfacial slip and an interfacial permeability that characterize the transport of fluid in the transition region around the interface between the porous flow and the viscous flow.

One of the salient features of these two-phase flow models is that both phases share a pressure field that amounts to the averaged spherical (isotropic) part of the microscopic stresses [11]. In each phase the extra (or additional) stress beyond the pressure may consist of shear or elastic stresses depending on the constitutive laws for each phase.

Theoretical analyses on the behavior and properties of a fully saturated (pore space completely filled with fluid) poro-elastic or poro-visco-elastic network have been conducted for either the Biot system (where the inertia of the poro-elastic and/or poro-visco-elastic skeleton may be important [2, 12]) or a similar Darcy poroelastic flow [13–17]. Modeled as a two-phase flow, the existence of an equilibrium solution (essential for mathematical analysis but often assumed without justification [2]) in the poroelastic flow can be guaranteed using the free energy minimization principle [8]. Mori *et al.* illustrated that boundary conditions at the interface between a poroelastic fluid and a viscous Newtonian fluid can be obtained from minimizing the elastic free energy of the porous frame. In this work we will utilize the same minimization principle to derive velocity boundary conditions that behave consistently as the fluid volume fraction (porosity) goes to zero.

Without resorting to the free energy dissipation principle, it is tedious to find effective boundary conditions near the surface of such heterogeneous materials. This is because at the interface between a porous Darcy medium and a viscous Stokes flow, there is a transient region of Brinkman flow where the viscous dissipation is in balance with pressure gradient and friction forces [18]. As a result, the standard techniques of homogenization break down in this region, and careful asymptotics [18–21] is required to derive (from first principle) the boundary condition that encompasses the well-known Navier slip boundary condition [22–24] and many other similar boundary conditions in previous works [3, 25–40].

Motivated by the physical complexity and mathematical richness of a poroelastic fluid when it's driven by or strongly coupled with viscous fluid flow as in the cellular cytosol, in this work we use a two-phase flow model to investigate the small-deformation of a poroelastic drop under linear flows (i.e., flows where the fluid velocity depends linearly on the spatial coordinates.) The hydrodynamics of a viscous drop in linear flows has been well studied as a classic paradigm in fluid mechanics, where the drop shape dynamics is characterized by the viscosity contrast and the capillary number, which is the ratio of flow strength to surface tension [41, 42]. Under a linear flow a viscous drop with a large surface tension deforms slightly from the spherical shape, and the small-deformation theory [42] predicts a steady equilibrium that has been validated by comparison with experiments and numerical simulations [41].

The motion of a spherical non-deformable porous drop freely suspended in a Stokes flow has been investigated [43–46]. The surface tension, essential for a spherical (or nearly spherical) viscous drop under linear flows, is replaced by the rigidity of the interior skeleton that is sufficiently strong to maintain a spherical shape with permeability on the interface.

Thus the boundary conditions for a non-deformable porous drop are continuity of velocity (both tangential and normal components) and normal stress, different from those of a non-deformable viscous drop where the normal velocity of the drop surface has to vanish in equilibrium [42]. With the rigid skeleton fully saturated (pore space completely filled with fluid) the drag coefficient and total force are computed as a function of the interior porosity in various flowing conditions such as a streaming flow, uniaxial extensional flow, and a planar shear flow. In addition the migration of a spherical porous drop in a planar shear flow or near a flat fluid interface has also been investigated [45].

To our knowledge no theoretical study has been conducted on the hydrodynamics of a deformable porous drop under linear flows. This may be partly due to the lack of boundary conditions on the interface between a poroelastic flow and a Stokes flow. The nonlinear coupling between the skeleton and the viscous fluid also adds another layer of difficulty to such theoretical study. Both factors contribute to the numerical design of an immersed boundary treatment of the skeleton-fluid interactions [9, 10].

In this work we focus on the hydrodynamics of a deformable poroelastic drop suspended in a viscous Stokes flow under two flowing conditions: a uniaxial extension flow and a planar shear flow. We focus on these two special linear flows here but our formulation is valid for any extensional viscous flow. By a "poroelastic drop" we refer to a finite volume that contains an elastic skeleton fully saturated with a viscous fluid. Specifically we assume that the skeleton pore space is filled with the same viscous fluid as the exterior fluid, thus exterior and interior fluid viscosities are the same and there is no surface tension on the interface.

In § II we formulate the two-phase flow model for a poroelastic flow coupled to a Stokes flow through the boundary defined by the edge of the skeleton phase. In the most general formulation the governing equations for the interior fluid phase are the Brinkmann equations where the viscous stress in the fluid is kept together with the pressure gradient and a frictional force between the fluid and the skeleton. After discussing the scalings for our problem we will specialize the general model to the Darcy flow case where the viscous fluid stress is small and negligible (compared to the pressure gradient and the frictional force) in the poroelastic drop. In § II B we derive the boundary conditions on the drop by free energy dissipation principle. Our boundary conditions differ from those in Mori *et al.* [8] in that the tangential component of the velocity boundary conditions are the generalized Navier slip boundary conditions. Using these boundary conditions and focusing on a poroelastic Darcy drop, in § III we investigate how a poroelastic Darcy drop undergoes small deformation when it is immersed in a uniaxial extensional flow and a planar shear flow. In particular we calculate the flow pattern and examine how the boundary conditions and poroelasticity affects the flow in and around the drop.

II. FORMULATION

Our problem is to study the dynamics of a poroelastic drop immersed in a Stokesian fluid acted upon by an applied flow. Let Ω_I represent the region of the drop, Ω_E the region of the exterior Stokes fluid, and Γ_t the interface between the poroelastic drop and the Stokesian fluid that evolves with time t, see Figure 1. Inside the poroelastic drop there are two phases:

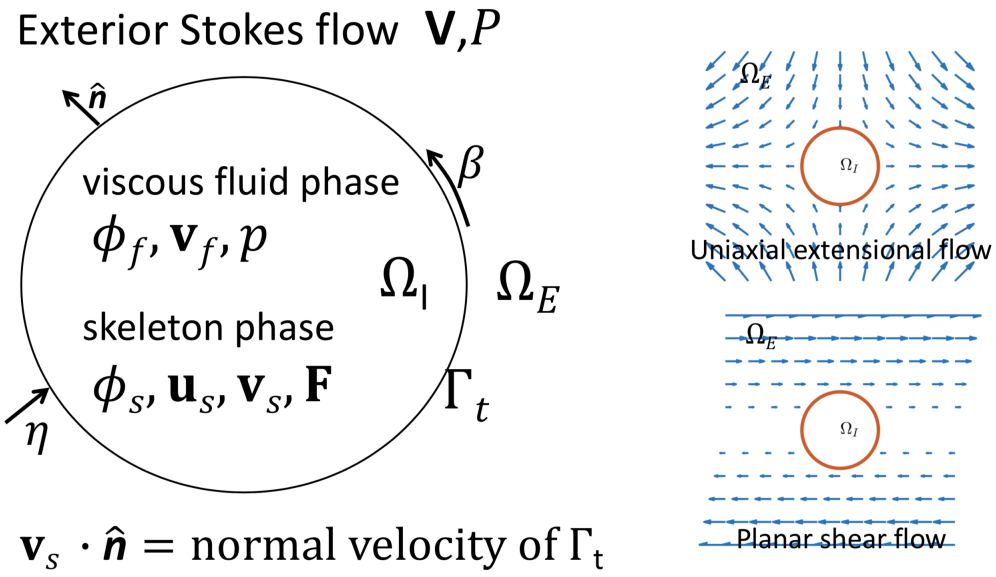

FIG. 1. *Left*: Sketch of a poroelastic drop (in Ω_I) immersed in a Stokesian fluid (in Ω_E). Inside the drop there is a fluid phase (subscript 'f') and a skeleton phase (subscript 's') which is bounded by the deformable interface Γ_t. $\hat{\mathbf{n}}$ is the outward normal, β is the interfacial slip coefficient, and η is the interfacial permeability. *Right*: A uniaxial extensional flow in the far-field (top) and a planar shear flow in the far-field (bottom).

a skeleton phase (subscript 's') and a fluid phase (subscript 'f'). The skeleton phase is confined within Ω_I, while the fluid may permeate in or out of the boundary Γ_t. Cartesian coordinates centered at the initial drop center will be denoted by (x, y, z), and spherical coordinates by (r, θ, ϕ), where $\theta \in [0, \pi]$ is the polar angle and $\phi \in [0, 2\pi]$ is the azimuthal angle.

A. Two-phase flow model

We start by assuming that a soft poro-elastic drop is freely suspended in a Newtonian viscous fluid with the velocity $\mathbf{V}$ and pressure P satisfying the incompressible Stokes equations

$$\mu \nabla^2 \mathbf{V} - \nabla P \equiv \nabla \cdot (2\mu \mathbf{E}) - \nabla P = 0, \tag{1}$$

$$\nabla \cdot \mathbf{V} = 0, \tag{2}$$

where μ is the viscosity of the exterior fluid and $\mathbf{E} \equiv \left(\nabla \mathbf{V} + (\nabla \mathbf{V})^T\right)/2$ is the strain rate tensor of the exterior fluid.

Inside the drop a deformable elastic skeleton is assumed to be fully hydrated, filled with the same viscous fluid of viscosity μ as the outside. The mixture of the elastic skeleton and the interior viscous fluid is coarse-grained into a two-phase flow, with the skeleton phase of volume fraction ϕ_s the fluid phase of volume fraction (porosity or void fraction) ϕ_f, and $\phi_f + \phi_s = 1$.

Conservation of the interior fluid and skeleton phases gives

$$\frac{\partial \phi_f}{\partial t} + \nabla \cdot (\phi_f \mathbf{v}_f) = 0, \tag{3}$$

$$\frac{\partial \phi_s}{\partial t} + \nabla \cdot (\phi_s \mathbf{v}_s) = 0, \tag{4}$$

with $\mathbf{v}_f$ the fluid velocity and $\mathbf{v}_s = d\mathbf{u}_s/dt$ the skeleton velocity, computed from taking the time derivative of the skeleton displacement $\mathbf{u}_s$. We note that in general the flow field in each phase is not necessarily incompressible ($\nabla \cdot \mathbf{v}_f \neq 0$ and $\nabla \cdot \mathbf{v}_s \neq 0$) when the fluid volume fraction (porosity or void fraction) ϕ_f has its own dynamics and may vary in space [11]. However, adding Equations (3) and (4) we identify an average local velocity $\mathbf{q} \equiv \phi_f \mathbf{v}_f + (1 - \phi_f)\, \mathbf{v}_s$ that is incompressible:

$$\nabla \cdot \mathbf{q} = \nabla \cdot (\phi_f \mathbf{v}_f + (1 - \phi_f)\, \mathbf{v}_s) = 0. \tag{5}$$

Denoting the extra stress [11] in the skeleton phase as σ_s and the strain rate tensor of the interior fluid phase as $\mathbf{e}_f \equiv (1/2)\left(\nabla \mathbf{v}_f + (\nabla \mathbf{v}_f)^T\right)$, the governing equations for the mixture of viscous fluid and poroelastic skeleton within the drop are [7, 8, 11, 47]

$$\nabla \cdot (\phi_f\, (2\mu \mathbf{e}_f)) - \phi_f \nabla p + \mathcal{F}^{s \to f} = 0, \tag{6}$$

$$\nabla \cdot (\phi_s \sigma_s) - \phi_s \nabla p + \mathcal{F}^{f \to s} = 0, \tag{7}$$

where $\mathcal{F}^{s \to f}$ is the force from the skeleton to the fluid and $\mathcal{F}^{f \to s} = -\mathcal{F}^{s \to f}$ is the anti-force from the fluid to the skeleton. Homogenization theory of a non-deformable porous medium filled with a viscous Stokes flow (zero Reynolds number) [1] shows that these forces are simplify the friction between the interior fluid and the skeleton (when there is no mechano-chemical process involved). In this work we assume that it is appropriate to generalize this drag force in a non-deformable porous medium to a frictional force in deformable porous medium as

$$\mathcal{F}^{s \to f} = -\xi \phi_f \phi_s\, (\mathbf{v}_f - \mathbf{v}_s) = -\mathcal{F}^{f \to s}, \tag{8}$$

where ξ is the drag coefficient assumed to be constant.

In general the extra stress σ_s (beyond the pressure in the skeleton phase) consists of both a viscous stress σ_v (that depends on the gradient of the rate of strain $\mathbf{v}_s$) and an elastic stress σ_e (that depends on the gradient of the displacement $\mathbf{u}_s$ of the elastic skeleton) [7, 8, 48]: $\sigma_s = \sigma_v(\nabla \mathbf{v}_s) + \sigma_e(\nabla \mathbf{u}_s)$. In this work we ignore the viscous stress of the skeleton ($\sigma_v = 0$).

For the elastic stress σ_e we adopt linear elasticity

$$\sigma_e = \mathbf{\Lambda} \mathrm{tr}(\varepsilon) \mathbf{I} + (\mathcal{M} - \mathbf{\Lambda}) \varepsilon, \tag{9}$$

where the strain

$$\varepsilon = \frac{1}{2}\left[\nabla \mathbf{u}_s + (\nabla \mathbf{u}_s)^T\right] \tag{10}$$

is assumed to be of small magnitude, suitable for the small-deformation analysis. In equation (9) $\mathcal{M}$ is the p-wave modulus and $\mathbf{\Lambda}$ is the Lamé's first parameter. In general $\mathcal{M} > \mathbf{\Lambda}$

and the Poisson ratio of the elastic skeleton is $\nu \equiv \mathbf{\Lambda}/(\mathcal{M}+\mathbf{\Lambda})$. A consequence of the small-strain assumption is that the deformation gradient tensor (in Eulerian frame)

$$\mathbf{F} \equiv (\mathbf{I} - \nabla \mathbf{u_s})^{-1} \approx \mathbf{I} + \nabla \mathbf{u_s}. \tag{11}$$

The corresponding fluid volume fraction (porosity) ϕ_f can be expressed as

$$\frac{\phi_f - \phi_0}{1-\phi_0} \approx \nabla \cdot \mathbf{u}_s \sim \epsilon \ll 1, \tag{12}$$

where ϕ_0 is the uniform fluid volume fraction distribution prior to the perturbation.

In this work we focus on cases where the viscous fluid outside the poroelastic drop is the same as the interior viscous fluid that fills up the space in the deformable elastic skeleton, thus there is no surface tension on Γ_t.

In this two-phase flow formulation the interior pressure p is determined by enforcing the incompressibility constraint in equation (5). As a result the pressure gradient is weighted to give the force in equations (6) and (7). Such formulation is consistent with previous work [7, 8, 11] where the volume fractions are outside (instead of inside) the gradient operator. As will be shown in § II B, the boundary conditions consistent with the free energy dissipation principle can be derived if the pressure gradient is weighted. No such consistent boundary conditions can be found if the volume fractions are inside the gradient operator.

B. Boundary Conditions

The boundary conditions at the interface between two homogeneous phases are usually derived by enforcing the conservation of mass and continuity of stress across the interface. This will be done here but these conditions are not sufficient for our multiphase drop. The difficulty is because we are connecting a single phase region with a two-phase region and we are considering only the macroscopic scale of the drop, i.e., the pore scale dynamics is coare-grained in the biphasic model. The free energy dissipation principle will be used to derive the additional boundary conditions.

Ignoring the surface tension the "interface" Γ_t here is the boundary that encloses all the elastic skeleton in Ω_I. Defined as such, the boundary Γ_t moves with velocity v_{Γ_t} determined only by the skeleton phase of the interior since the fluid phase is permeable to the boundary. Thus, instead of the usual kinematic boundary condition where the time derivative of Γ_t is equal to the normal component of the fluid velocity evaluated on Γ_t, our first boundary condition is the kinematic condition for a permeable interface with a skeleton inside:

$$\mathbf{v}_s\Big|_{\Gamma_t} \cdot \hat{\mathbf{n}} = v_{\Gamma_t}. \tag{13}$$

Conservation of fluid mass at the interface Γ_t demands that the mass of fluid leaving the poroelastic drop in the normal direction from Ω_I balance the mass of fluid entering the region Ω_E. Since the fluids are incompressible and the same in both regions we find that,

$$(\mathbf{V} - \mathbf{v}_s)\Big|_{\Gamma_t} \cdot \hat{\mathbf{n}} = \phi_f\,(\mathbf{v}_f - \mathbf{v}_s)\Big|_{\Gamma_t} \cdot \hat{\mathbf{n}}. \tag{14}$$

Continuity of stress at the interface requires the total stress balance:

$$\left(-2\mu\mathbf{E} + P\mathbf{I} + \phi_f(2\mu\mathbf{e}_f) + \phi_s\sigma_s - p\mathbf{I}\right)\Big|_{\Gamma_t} \cdot \hat{\mathbf{n}} = 0. \tag{15}$$

Hou *et al.* [32] derived a similar boundary condition when the flow Reynolds number is sufficiently large for the momentum flux term to be important in the stress balance. This term can be ignored in the low Reynolds number (Stokes flow) limit we are working in. Equations (14)-(15) are not sufficient to find a unique solution to the problem.

In order to find the additional boundary conditions we begin by integrating the product of $\mathbf{V}$, $\mathbf{v}_f$ and $\mathbf{v}_s = d\mathbf{u}_s/dt$ with equations (1), (6), and (7), respectively, over the whole region $\Omega = \Omega_E + \Omega_I$. Use (2), (3), (4) and apply the divergence theorem to find:

$$\begin{aligned} 0 &= \int_{\Omega_E} \mathbf{V} \cdot \left[\nabla(2\mu\mathbf{E}) - \nabla P\right] d^3x \qquad (16)\\ &+ \int_{\Omega_I} \mathbf{v}_f \cdot \left[\nabla(\phi_f\,(2\mu\mathbf{e}_f)) - \phi_f\nabla p - \xi\phi_f\phi_s(\mathbf{v}_f - \mathbf{v}_s)\right] d^3x \\ &+ \int_{\Omega_I} \mathbf{v}_s \cdot \left[\nabla\cdot(\phi_s\sigma_s) - \phi_s\nabla p + \xi\phi_f\phi_s(\mathbf{v}_f - \mathbf{v}_s)\right] d^3x \\ &= \int_{\Gamma_t} -\mathbf{V}\cdot(2\mu\mathbf{E} - P\mathbf{I})\cdot\hat{\mathbf{n}}ds + \int_{\Gamma_t} \mathbf{u}_f \cdot (\phi_f\,(2\mu\mathbf{e}_f) - \phi_f p\mathbf{I})\hat{\mathbf{n}}ds \qquad (17)\\ &+ \int_{\Gamma_t} \mathbf{v}_s \cdot (\phi_s\sigma_s - \phi_s p\mathbf{I})\hat{\mathbf{n}}ds - I_{\Omega_E} - I_{\Omega_I} - I_E, \end{aligned}$$

where

$$I_{\Omega_E} = \int_{\Omega_E} 2\mu\mathbf{E} : \nabla\mathbf{V} d^3x \tag{18}$$

$$I_{\Omega_I} = \int_{\Omega_I} \phi_f(2\mu\mathbf{e}_f) : \nabla\mathbf{v}_f + \xi\phi_f\phi_s \left\|\mathbf{v}_f - \mathbf{v}_s\right\|^2 d^3x, \tag{19}$$

$$I_E = \int_{\Omega_I} \phi_s\sigma_e\left(\nabla\mathbf{u}_s\right) : \nabla\mathbf{v}_s d^3x. \tag{20}$$

Here we have assumed that the surface integrals along the outer boundary of Ω_E are zero. This would be true for an applied flow where at this outer boundary the pressure balances the applied strain or for a flow where $\mathbf{V}$ tends to zero. After integration by parts, equation (17) shows that the sum of the three surface integrals on Γ_t and the two volume integrals I_{Ω_E} and I_{Ω_I} must equal to the volume integral I_E, which has been shown to be equal to the rate of change of an elastic free energy $\mathcal{E}_{elas}$ [8]:

$$\begin{aligned} I_E = \frac{d\mathcal{E}_{elas}}{dt} &= \int_{\Gamma_t} -\mathbf{V}\cdot(2\mu\mathbf{E} - P\mathbf{I})\cdot\hat{\mathbf{n}}ds + \int_{\Gamma_t} \mathbf{v}_f\cdot(\phi_f\,(2\mu\mathbf{e}_f) - \phi_f p\mathbf{I})\hat{\mathbf{n}}ds \\ &+ \int_{\Gamma_t} \mathbf{v}_s\cdot(\phi_s\sigma_s - \phi_s p\mathbf{I})\hat{\mathbf{n}}ds - I_{\Omega_E} - I_{\Omega_I}, \end{aligned} \tag{21}$$

where

$$\mathcal{E}_{elas} = \int_{\Omega_I} \phi_s\mathcal{W}_{elas}(\mathbf{F})d^3x, \quad \text{with } \sigma_e(\mathbf{u}_s) = \frac{\partial\mathcal{W}_{elas}(\mathbf{F})}{\partial\mathbf{F}}\mathbf{F}^T, \tag{22}$$

where $\phi_s \mathcal{W}_{elas}$ is elastic energy per unit volume and $\mathbf{F}$ is the gradient of deformation tensor defined in Equation (11). Derivation of the identity $I_E = d\mathcal{E}_{elas}/dt$ can be found in Mori *et al.* [8], Antman [49] and Gurtin *et al.* [50]. It is straightforward to show that the volume integrals are positive definite, thus one way to ensure $d\mathcal{E}_{elas}/dt < 0$ is to choose boundary conditions such that the righthand side of Equation (21) is negative. The minimal free energy principle [49, 50] and this observation can then be used to derive the boundary conditions. We note that if the volume fractions are inside the gradient operator in Equations (6-7) ($\nabla(\phi_f p)$ instead of $\phi_f \nabla p$), then after integration by parts there will be a volume integral that is not positive definite, and no boundary conditions can be chosen to satisfy the free energy dissipation principle.

Focusing on the surface integrals, denote the velocities relative to the skeleton velocity $\mathbf{v}_s$ with a bar as

$$\overline{\mathbf{V}} = \mathbf{V} - \mathbf{v}_s, \quad \overline{\mathbf{v}}_f = \phi_f(\mathbf{v}_f - \mathbf{v}_s), \tag{23}$$

the surface integrals in Equation (21) are thus recast as

$$\begin{aligned}
&\int_{\Gamma_t} -(\overline{\mathbf{V}} + \mathbf{v}_s)(2\mu\mathbf{E} - P\mathbf{I})\hat{\mathbf{n}} + \left(\frac{\overline{\mathbf{v}}_f}{\phi_f} + \mathbf{v}_s\right)(\phi_f(2\mu\mathbf{e}_f) - \phi_f p\mathbf{I})\hat{\mathbf{n}} + \mathbf{v}_s\left(\phi_s\sigma_s - \phi_s p\mathbf{I}\right)\hat{\mathbf{n}} ds \\
&= \int_{\Gamma_t} \mathbf{v}_s \cdot (-2\mu\mathbf{E} + P\mathbf{I} + \phi_f(2\mu\mathbf{e}_f) + \phi_s\sigma_s - p\mathbf{I})\hat{\mathbf{n}} ds + \qquad (24a) \\
&\int_{\Gamma_t} -\overline{\mathbf{V}} \cdot (2\mu\mathbf{E} - P\mathbf{I})\hat{\mathbf{n}} + \overline{\mathbf{v}}_f \cdot (2\mu\mathbf{e}_f - p\mathbf{I})\hat{\mathbf{n}} ds. \qquad (24b)
\end{aligned}$$

Using the stress boundary condition Equation (15) we find that Equation (24a) is zero. We note that when the drop interior is a single fluid phase ($\phi_f = 1$ and $\phi_s = 0$), the integral in Equation (24b) vanishes because of velocity continuity $\overline{\mathbf{V}} = \overline{\mathbf{v}}_f$. In the more general cases $\phi_f \in (0, 1)$ and the drop interior consists of two phases, more boundary conditions need to be derived from the integral in Equation (24b).

To proceed further, we decompose $\overline{\mathbf{V}}$ and $\overline{\mathbf{v}}_f$ into the parallel (subscript '$\parallel$') and perpendicular (subscript '$\perp$') to the interface Γ_t as

$$\overline{\mathbf{V}} = \overline{\mathbf{V}}_\perp + \overline{\mathbf{V}}_\parallel, \quad \overline{\mathbf{v}}_f = \overline{\mathbf{v}}_{f\perp} + \overline{\mathbf{v}}_{f\parallel}. \tag{25}$$

Conservation of fluid mass from Equation (14) gives $\overline{\mathbf{V}}_\perp = \overline{\mathbf{v}}_{f\perp}$. To make the normal velocity component of (24b) negative definite, a simple choice is to choose $\eta > 0$ such that

$$\overline{\mathbf{V}}_\perp = \eta \left\{ \hat{\mathbf{n}} \cdot (2\mu\mathbf{E} - P\mathbf{I} - 2\mu\mathbf{e}_f + p\mathbf{I})\Big|_{\Gamma_t} \cdot \hat{\mathbf{n}} \right\} \hat{\mathbf{n}}. \tag{26}$$

For the tangential component, choices for $\overline{\mathbf{V}}_\parallel$ and $\overline{\mathbf{v}}_{f\parallel}$ must be made based on the condition that the integral in Equation (24b) must be semi-negative definite. One way to achieve that is the following generalized Navier slip (which is found at the boundary between a

Stokes flow and a permeable Darcy medium [22, 24]):

$$\overline{\mathbf{V}}_{\parallel} = \beta \left(\mu \mathbf{E}\Big|_{\Gamma_t} \cdot \hat{\mathbf{n}} \right)_{\parallel}, \tag{27}$$

$$\overline{\mathbf{v}}_{f\parallel} = -\beta \left(\mu \mathbf{e}_f\Big|_{\Gamma_t} \cdot \hat{\mathbf{n}} \right)_{\parallel}. \tag{28}$$

Note that in Darcy flow limit of small viscous stress, equation (28) will naturally disappear as the last term in the surface integral in equation (24b) vanishes.

In summary, the boundary conditions for $\mathbf{V}$, $\mathbf{v}_f$ and $\mathbf{v}_s$ are given by (14), (15), (26), and (27). For future reference these can be collected here as:

$$\left[(\mathbf{V} - \mathbf{v}_s) - \phi_f \left(\mathbf{v}_f - \mathbf{v}_s \right) \right] |_{\Gamma_t} \cdot \hat{\mathbf{n}} = 0, \tag{29}$$

$$(\mathbf{V} - \mathbf{v}_s) |_{\Gamma_t} \cdot \hat{\mathbf{n}} = \eta \hat{\mathbf{n}} \cdot \left[(2\mu \mathbf{E} - P\mathbf{I}) - (2\mu \mathbf{e}_f - p\mathbf{I}) \right] |_{\Gamma_t} \cdot \hat{\mathbf{n}}, \tag{30}$$

$$(\mathbf{V} - \mathbf{v}_s) |_{\Gamma_t} \cdot \hat{\mathbf{t}} = \beta \hat{\mathbf{n}} \cdot \mu \mathbf{E}|_{\Gamma_t} \cdot \hat{\mathbf{t}}, \tag{31}$$

$$\phi_f \left(\mathbf{v}_f - \mathbf{v}_s \right) |_{\Gamma_t} \cdot \hat{\mathbf{t}} = -\beta \hat{\mathbf{n}} \cdot \mu \mathbf{e}_f|_{\Gamma_t} \cdot \hat{\mathbf{t}}, \tag{32}$$

$$\hat{\mathbf{n}} \cdot \left[(2\mu \mathbf{E} - P\mathbf{I}) - (\phi_s \sigma_s + \phi_f (2\mu \mathbf{e}_f) - p\mathbf{I}) \right] |_{\Gamma_t} \cdot \hat{\mathbf{n}} = 0, \tag{33}$$

$$\hat{\mathbf{t}} \cdot \left[2\mu \mathbf{E} - (\phi_s \sigma_s + \phi_f \left(2\mu \mathbf{e}_f \right)) \right] |_{\Gamma_t} \cdot \hat{\mathbf{n}} = 0, \tag{34}$$

where $\sigma_s = \sigma_e$ is the linear elastic stress given in equation (9). $\eta > 0$ is an interfacial permeability, and $\beta > 0$ is an interfacial slip coefficient. Equations (31)-(32) are consistent with the slip boundary condition derived by Angot *et al.* [18], and it is shown to be compatible with models previously derived for different configurations [18]. For a permeable moving boundary, the normal component of the total stress is from the fluid pressure and the shear component must vanish; this implies that both the normal and shear components of the effective stress must vanish. Equations (33)-(34) are for the stress balance at the boundary (more general than either permeable or impermeable boundaries) between a two-phase flow and a viscous Stokes flow. These are similar to the stress balance at the boundary between a polyelectrolyte gel and a Stokes flow in Mori *et al.* [8].

C. External linear flow field

For later reference it will be helpful to recall that for axi-symmetric incompressible flows around a fluid drop there exists a stream function ψ_e for the exterior fluid flow

$$V_r = -\frac{1}{r^2 \sin\theta} \frac{\partial \psi_e}{\partial \theta}, \; V_\theta = \frac{1}{r \sin\theta} \frac{\partial \psi_e}{\partial r}, \;\; V_\phi = 0. \tag{35}$$

Here we will compare the flow around a viscous drop and a Darcy drop in both a planar shear flow and a uniaxial extensional flow. For a uniaxial extensional flow the far-field fluid velocity is

$$\mathbf{V} \to -E\left(x, y, -2z\right) = -Ex\hat{\mathbf{i}} - Ey\hat{\mathbf{j}} + 2Ez\hat{\mathbf{k}} \text{ as } r \to \infty, \tag{36}$$

where E is the extension rate. $\hat{\mathbf{i}}$, $\hat{\mathbf{j}}$ and $\hat{\mathbf{k}}$ are the unit vectors in the Cartesian coordinates. For a planar shear flow the far-field fluid velocity is

$$\mathbf{V} \to \dot{\gamma}(y, 0, 0) = \dot{\gamma} y \hat{\mathbf{i}} \text{ as } r \to \infty, \tag{37}$$

where $\dot{\gamma}$ is the shear rate of the background planar shear flow. We will apply the two-phase model to a slightly deformable porous drop.

D. Scaling and Non-dimensionalization

Here we will discuss the scaling of some of our parameters and introduce dimensionless variables into the equations (1)-(8) and boundary conditions in equations (29)-(34). The characteristic length scale is given by the drop radius l_0. The characteristic time scale is given by $t_e \equiv \xi l_0^2/\mathcal{M}$ (based on the elastic modulus and friction coefficient), and the characteristic pressure is $\mathcal{M}$. Note that this allows us to define a characteristic velocity $v_e \equiv \mathcal{M}/(\xi l_0)$. It should be remembered that a basic assumption to justify the use of the two-phase flow model as used here is that the average pore size a_0 is much smaller than l_0, i.e. $a_0/l_0 \ll 1$. In the scaling below we will assume $a_0 = 0.1 \sim 1\mu m$ and $10\mu m \leq l_0 \leq 1mm$, which is consistent with the two-phase flow modeling.

The effective media theory[1] provides a simple estimate for the drag coefficient as $\xi \sim \mu/a_0^2$. The range for ξ can be computed as $10^9 \frac{kg}{m^3 s} \leq \xi \leq 10^{15} \frac{kg}{m^3 s}$, where the lower bound corresponds to a porous medium (with average pore size $a_0 = 0.1 \sim 1\ \mu m$) filled with water ($\mu = 10^{-3} Pas$). The upper bound corresponds to the articular cartilage in normal human knee [51–54]. Neglecting the re-arrangement of solid phase due to the flow near the boundary, we may estimate the interfacial permeability as $\eta \sim 1/(l_0 \xi)$ and obtain the range of η as: $10^{-10} \frac{m^2 s}{kg} \leq \eta \leq 10^{-4} \frac{m^2 s}{kg}$. We note that the water permeability constant for a biological cellular membrane is of the order $10^{-10} \frac{m^2 s}{kg}$ (see Li *et al.* [55] and references therein). The Lamé coefficients are often between KPa (for hydrogels) and MPa (for articular cartilage) with a Poisson ratio around 0.2. The interfacial slip β is proportional to the average pore size for hydrophilic surfaces [22]: $\beta \sim a_0/l_0 \ll 1$. For hydrophobic surfaces (or surfaces treated with hydrophobic agents) the slip length can be much larger than the pore size [56–58]. In this work we will explore a wide range of β and η and examine their effects on the flow around a deformable poroelastic drop. Finally note that for a poroelastic drop of radius $l_0 = 10\ \mu m$ is filled with articulate cartilage, $t_e \sim 0.1 s$ and $v_e \sim 100\ \mu m/s$.

The dimensionless parameters for the poroelastic drop are $\bar{\Lambda} = \Lambda/\mathcal{M}$, $\bar{\alpha}_e = \mu v_e/\mathcal{M} l_0 = \mu/(\xi l_0^2)$, slip coefficient $\bar{\beta} = \beta\mu/l_0 = \bar{\alpha}_e \beta \mathcal{M}/v_e$, and permeability $\bar{\eta} = \eta \mathcal{M}/v_e$. For the extension flow the dimensionless extension rate is $\bar{E} = E\xi l_0^2/\mathcal{M}$, and for the simple shear flow the dimensionless shear rate is $\bar{\dot{\gamma}} = \dot{\gamma}\xi l_0^2/\mathcal{M}$. These are just the ratios fo the time scales of the applied flow ($1/\dot{\gamma}$ and $1/E$) to t_e. Our analysis assumes a small deformation of the elastic skeleton. This assumption is valid for small applied flow where our analysis is applicable, but it is also valid for a poroelastic drop with strong bending moduli under large applied flow. Thus without loss of generality we will set $\bar{E} = 1$ and $\bar{\dot{\gamma}} = 1$.

As noted earlier, our plan is to focus on the Darcy flow limit within the drop. This means that the viscous fluid stress is small in the poroelastic drop and will be neglected in

equations (1)-(8). The resultant dimensionless equations (after dropping the bar) for the Darcy-Stokes system are

$$\alpha_e \nabla^2 \mathbf{V} - \nabla P = 0, \tag{38}$$

$$\nabla \cdot \mathbf{V} = 0, \tag{39}$$

$$-\phi_f \nabla p - \phi_f \phi_s \left(\mathbf{v}_f - \mathbf{v}_s\right) = 0, \tag{40}$$

$$\nabla \cdot (\phi_s \sigma_e) - \phi_s \nabla p + \phi_s \phi_f \left(\mathbf{v}_f - \mathbf{v}_s\right) = 0, \tag{41}$$

$$\frac{\partial \phi_f}{\partial t} + \nabla \cdot (\phi_f \mathbf{v}_f) = 0, \tag{42}$$

$$\phi_f + \phi_s = 1, \quad \nabla \cdot (\phi_f \mathbf{v}_f + \phi_s \mathbf{v}_s) = 0. \tag{43}$$

The corresponding dimensionless boundary conditions on the interface Γ_t are

$$\left[\left(\mathbf{V} - \mathbf{v}_s\right) - \phi_f \left(\mathbf{v}_f - \mathbf{v}_s\right)\right]|_{\Gamma_t} \cdot \hat{\mathbf{n}} = 0, \tag{44}$$

$$\left(\mathbf{V} - \mathbf{v}_s\right)|_{\Gamma_t} \cdot \hat{\mathbf{n}} = \eta \hat{\mathbf{n}} \cdot \left[\left(2\alpha_e \mathbf{E} - P\mathbf{I}\right) - \left(-p\mathbf{I}\right)\right]|_{\Gamma_t} \cdot \hat{\mathbf{n}}, \tag{45}$$

$$\left(\mathbf{V} - \mathbf{v}_s\right)|_{\Gamma_t} \cdot \hat{\mathbf{t}} = \beta \hat{\mathbf{n}} \cdot \mathbf{E}|_{\Gamma_t} \cdot \hat{\mathbf{t}}, \tag{46}$$

$$\hat{\mathbf{n}} \cdot \left[\left(2\alpha_e \mathbf{E} - P\mathbf{I}\right) - \left(\phi_s \sigma_e - p\mathbf{I}\right)\right]|_{\Gamma_t} \cdot \hat{\mathbf{n}} = 0, \tag{47}$$

$$\hat{\mathbf{t}} \cdot \left[2\alpha_e \mathbf{E} - \phi_s \sigma_e\right]|_{\Gamma_t} \cdot \hat{\mathbf{n}} = 0. \tag{48}$$

In this work we focus on the Darcy regime where the viscous dissipation in equation (6) is negligible compared to the pressure gradient and the friction force. As stated in § I the fluid flow through and around a Darcy medium has been previously investigated without considering the effects of both the external viscous stress and the deformation of the porous network in the medium, which is the focus of the present work.

When the viscous dissipation is retained the governing equations are for the flow through a deformable Brinkmann medium, which is more appropriate for low solid volume fraction [1] $\phi_s \leq\sim 5\%$. We are now conducting active investigation on this system and results will be summarized in a subsequent paper.

In this work we neglect the surface tension and focus on the Darcy regime, where a deformable Darcy drop is freely suspended in (1) a uniaxial extensional flow and (2) a planar shear flow. We focus on the physical regime where the elastic skeleton deforms slightly to contribute to the shape deviation of the drop from a sphere.

In such small-deformation limit the volume fraction of the elastic skeleton deviates very little from the original distribution. To elucidate the salient features of slip and permeability effects on the hydrodynamics of a soft poroelastic drop, we conduct a small-deformation analysis on a poroelastic drop of (nearly) an initially uniform porosity ϕ_0, and the nearly spherical drop shape is supported by a skeleton of large elastic modulus. The effects of non-uniform volume fraction (porosity) on the dynamics of an elastic poroelastic skeleton in one-dimension is the main focus of the work by MacMinn *et al.* [47]. It is a non-trivial extension to incorporate the non-uniform porosity into the small-deformation analysis. Based on results from MacMinn *et al.* [47] we expect to rely on numerical computations as analytical solutions may not be readily available for a system of boundary value problems with variable coefficients.

Finally we remark that in the limit of infinitely large network elastic moduli, the network becomes rigid (non-deformable) and both the displacement and the rate of strain vanish. Consequently less boundary conditions are needed in this non-deformable limit, and early works have focused on the balance of normal stress and continuity of the normal component of the fluid velocity [33, 46, 59].

III. SMALL-DEFORMATION OF A POROELASTIC DARCY DROP

In this section we investigate the flow around a poroelastic drop with large bending moduli such that the elastic skeleton (and hence the drop interface) undergoes small deformation from the initial spherical shape. On the interface Γ_t

$$r = 1 + \delta r(t, \theta, \phi) = 1 + \mathbf{u}_s \cdot \hat{\mathbf{r}}, \quad |\delta r| = |\mathbf{u}_s \cdot \hat{\mathbf{r}}| \ll 1. \tag{49}$$

For a viscous drop in a flow, strong surface tension (small capillary number) ensures the small deformation in Equation (49) is possible, and the drop responds linearly under a general linear flow [42]. For a poro-elastic drop, however, the nonlinear relationship between the solid phase flow field $\mathbf{v}_s$ and the deformation $\mathbf{u}_s$ requires us to assume further that the flow strength is small such that

$$\mathbf{v}_s = \frac{d\mathbf{u}_s}{dt} = \frac{\partial \mathbf{u}_s}{\partial t} + (\mathbf{v}_s \cdot \nabla)\, \mathbf{u}_s \approx \frac{\partial \mathbf{u}_s}{\partial t}. \tag{50}$$

In the literature many researchers adopted the above approximation in their modeling of a biphasic poroelastic fluid [48, 51, 60, 61]. Here we will assume that such approximation is sufficient to capture the small-deformation of a poroelastic drop under a linear flow. In our small-deformation analysis, the volume fractions ϕ_f and ϕ_s are assumed to be initially homogeneous with $\phi_f \approx \phi_0$. The deviation from the initial homogeneous distribution is related to the divergence of the displacement field in Equation (12). Outside the poroelastic drop the linear Stokes flow is coupled to the interior poroelastic flow via the boundary conditions evaluated at the unperturbed spherical interface in the small-deformation framework. This way the governing equations are a linear system that can still be solved using separation of variables.

From equations (40)-(43), the linearized Darcy equations and the governing equations for stress balance in the solid phase are

$$-\phi_0 \nabla p - \phi_0(1-\phi_0)\left(\mathbf{v}_f - \frac{\partial \mathbf{u}_s}{\partial t}\right) = 0, \tag{51}$$

$$\nabla \cdot ((1-\phi_0)\sigma_e(\mathbf{u}_s)) - \nabla p = 0, \tag{52}$$

$$\nabla \cdot (\phi_0 \mathbf{v}_f + (1-\phi_0)\mathbf{v}_s) = 0. \tag{53}$$

The general solution for the above linear equations take the following form

$$\begin{pmatrix} \mathbf{v}_f \\ \mathbf{v}_s \\ p \end{pmatrix} = \begin{pmatrix} \widehat{\mathbf{v}}_f \\ \widehat{\mathbf{v}}_s \\ \widehat{p} \end{pmatrix} + e^{\omega t} \begin{pmatrix} \mathbf{v}_{f,1} \\ \mathbf{v}_{s,1} \\ p_1 \end{pmatrix}, \tag{54}$$

where the hat symbol $\widehat{\cdot}$ denotes the steady equilibrium solution, and the subscripts "1" denotes the exponential components that vary with time at an exponential rate ω. In the following we will solve for both the steady equilibrium and the eigenvalue ω. Note that since in the small-deformation limit $\mathbf{v}_s = \widehat{\mathbf{v}}_s + e^{\omega t}\mathbf{v}_{s,1} \sim \partial \mathbf{u}_s/\partial t$, we can write $\mathbf{u}_s = \widehat{\mathbf{u}}_c(t) + e^{\omega t}\mathbf{u}_{s,1}$, where now $\widehat{\mathbf{u}}_c(t)$ can depend linearly on t.

A. Steady Equilibrium

Within the small-deformation regime, a viscous drop with a large surface tension (small capillary number) reaches a steady shape under linear flows. Similarly for a nearly spherical poroelastic drop with a large network rigidity, we assume that it reaches a steady shape under linear flows. At steady equilibrium the normal component of the skeleton velocity $\mathbf{v}_s$ evaluated at the steady drop interface is zero.

The tangential components of the network velocity, on the other hand, depends on the exterior flow condition: Under a uniaxial extensional flow the tangential network velocity is zero at steady equilibrium, while under a planar shear flow the tangential network velocity is a rigid-body rotation due to the rotational component of the far-field shear flow. For the linear shear flow, the network rotates due to the vorticity in the shear flow. This network rotation is a rigid-body rotation that does not cause any viscous dissipation. However, as we will shown in § III C, there is a non-trivial elastic stress in the skeleton phase in balance with the pressure gradient due to such rotation.

B. Uniaxial extension flow

First we identify the steady equilibrium solution for a Darcy drop under a uniaxial extensional flow specified by Equation (36). At steady equilibrium, the general solutions for the drop interior take the form

$$\widehat{p} = -\frac{7}{10}(1-\phi_0)(1-\Lambda)d_1 r^2\left(1+3\cos(2\theta)\right), \tag{55}$$

$$\widehat{\mathbf{u}}_s \cdot \hat{\mathbf{r}} = \left(-\frac{3(5-2\Lambda)}{25}d_1 r^3 - d_2 r - \frac{2\Lambda}{7+3\Lambda}d_3 r^3\right)\left(1+3\cos(2\theta)\right), \tag{56}$$

$$\widehat{\mathbf{u}}_s \cdot \hat{\theta} = \left(\frac{3(6-\Lambda)}{25}d_1 r^3 + d_2 r + \frac{1}{3}d_3 r^3\right)\sin(2\theta), \tag{57}$$

and $\widehat{\mathbf{v}}_s = 0$ in the case of a uniaxial extensional flow. Here $\hat{\mathbf{r}}$ and $\hat{\theta}$ are unit vectors in the r and θ directions. The solution for the exterior Stokes flow is

$$\widehat{\psi}_e = \left(r^3 - \frac{A_1}{2} - \frac{A_2}{2r^2}\right)\cos\theta\sin^2\theta, \tag{58}$$

$$\widehat{P}_e = -\frac{\alpha_e}{2r^3}A_1\left(1+3\cos(2\theta)\right), \tag{59}$$

where ψ_e is the stream function and P_e is the pressure for the external fluid. Altogether there are five coefficients (A_1, A_2, d_1, d_2, d_3) to be determined by the five boundary conditions

in Equations (44)-(48). We focus on parameter combinations that pertain to the small-deformation assumption. The expression for the five coefficients are given in Appendix B.

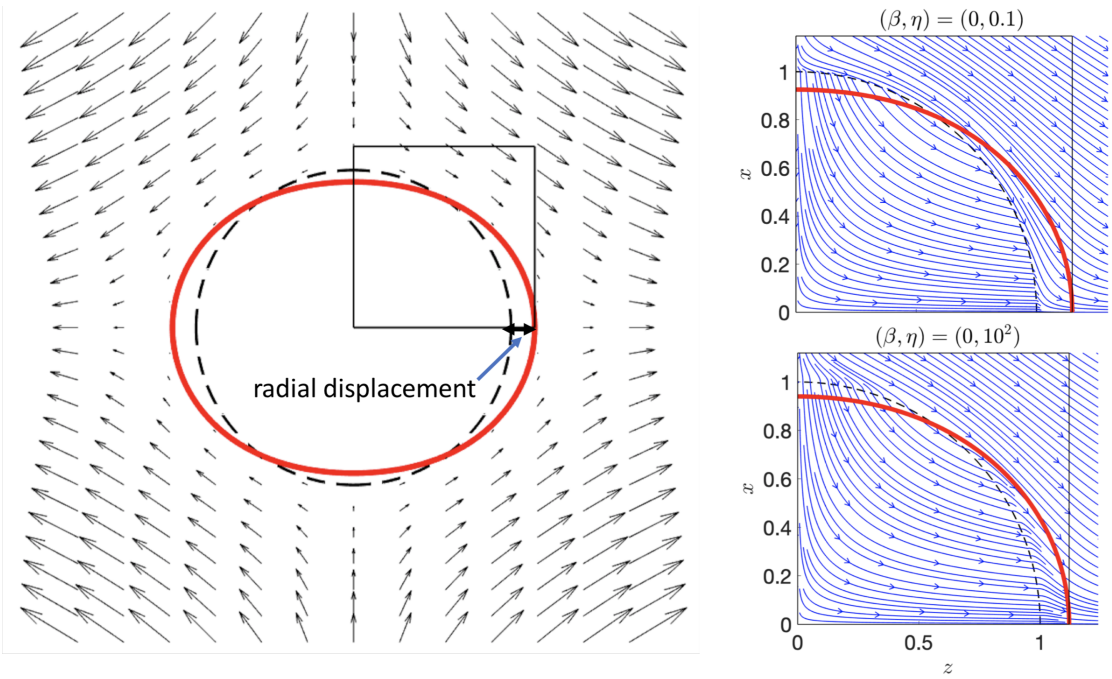

FIG. 2. *Left*: Illustration of a slightly deformed poroelastic drop under a uniaxial extensional flow. $\phi_0 = 0.5$, $\Lambda = 1/3$, and $\alpha_e = 0.005$. Dashed line is the original spherical drop shape. Thick solid line is the equilibrium drop shape. $(\beta, \eta) = (0, 0)$. *Right*: Stream lines in the first quadrant for two sets of (β, η) as labeled.

Figure 2 is a two-dimensional cross section ($x - z$ plane) of the equilibrium drop shape from the steady linear solutions in Equations (56)-(57) with $\Lambda = 1/3$, $\alpha_e = 5 \times 10^{-3}$ and $\phi_0 = 0.5$. On the $x - z$ plane, the uniaxial extensional flow (equation (36)) converges along the vertical (x) axis and diverges along horizontal (z) axis, as indicated by the arrows outside the drop. Starting from a spherical shape (dashed curve), the drop is compressed in the x-axis and stretched in the z-axis to the equilibrium shape (thick curve). The magnitude of radial displacement is defined as the maximum of deformation as illustrated.

Despite the similarity in the deformed shape between a poroelastic drop and a viscous drop (see figure 14 in Appendix A), the flow inside the drop is very different: For a viscous drop the exterior extension flow goes around the drop and an interior flow of four vortices is induced. The strength of the interior flow is inversely proportional to the viscosity contrast. The larger the interior viscosity the smaller the flow strength, as shown in figure 14. For a poroelastic drop the interior flow depends on the interfacial permeability η. When the interfacial permeability $\eta = 0$, there is no flow inside the drop and the extension flow goes around the drop as shown in the left of figure 2. This is similar to the large viscosity ratio limit case of figure 14(c). For non-zero interfacial permeability the flow can go into the drop around the pole and an interior flow develops as shown in the right panels, where the gradient of the stream function is discontinuous on the boundary because $\eta \neq 0$.

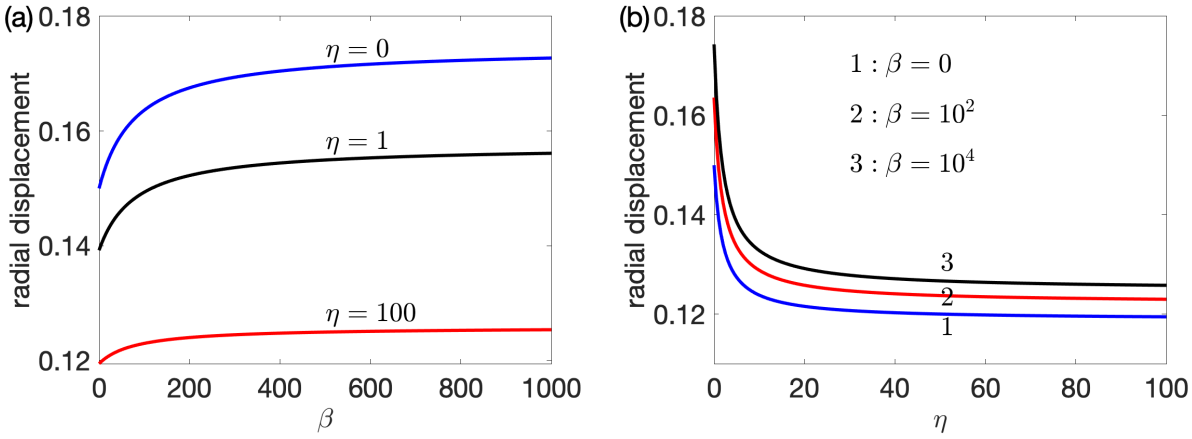

FIG. 3. Radial displacement ($\widehat{\mathbf{u}}_s \cdot \hat{\mathbf{r}}$) of a poroelastic drop in a uniaxial extensional flow. $\Lambda = 1/3$, $\phi_0 = 0.5$ and $\alpha_e = 0.005$. (a) radial displacement versus β for three values of η as labeled. (b) radial displacement versus η for three valeus of β as labeled.

The streamlines in the right panels of figure 14 (calculated from a matlab subroutine streamslice) show that the flow penetrates the drop around $x = 1$ (pole) and leaves the drop around $z = 1$ (equator). We note that, in the small-deformation framework, the velocity boundary conditions are evaluated at the unperturbed shape ($r = 1$, dashed curve in figure 2). The deformed shape is a consequence of such solution, which does not satisfy the boundary conditions on the deformed drop shape (thick curves in figure 2). Following the arrows of streamlines inside the drop from the pole to the equator, we observe that the flow turns more along the tangent along the drop boundary as it exits the drop. We also observe that, as η increases from 0.1 to 100, there is more flow going through the drop while a slightly smaller radial displacement is found.

Figure 3 shows the magnitude of equilibrium radial displacement plotted against β (panel (a)) and η (panel (b)) with $\Lambda = 1/3$, $\alpha_e = 0.005$ and $\phi_0 = 0.5$. For these parameter values, the radial displacement appears to depend only weakly on β as shown in figure 3(a). Note how the displacement asymptotes to an equilibrium value with increasing β and η. Note also how increasing the permeability η decreases the displacement. The slip effect on the equilibrium drop deformation under an extension flow has been investigated in various contexts: For a viscous drop the interfacial slip is found to always reduce the equilibrium drop deformation [62]. For a viscoelastic drop in a viscoelastic medium, the interfacial slip is found to increase the drop deformation [63]. Here we observe that the poroelastic drop behaves more like a viscoelastic drop when it comes to slip effect on the drop deformation.

Figure 4 shows the inflow in the first quadrant defined as

$$\text{inflow in first quadrant} = \frac{1}{2}\int_0^{2\pi}\int_0^{\pi/2} |\mathbf{V}|_{\Gamma_t} \cdot \hat{\mathbf{r}}| \sin\theta d\theta d\phi, \tag{60}$$

where the integral without the absolute sign would vanish due to symmetry of the perturbation, and hence the combination of factor 1/2 and the absolute value sign gives the net inflow, which is exactly equal to the out-flow in the first quadrant. We observe that the net

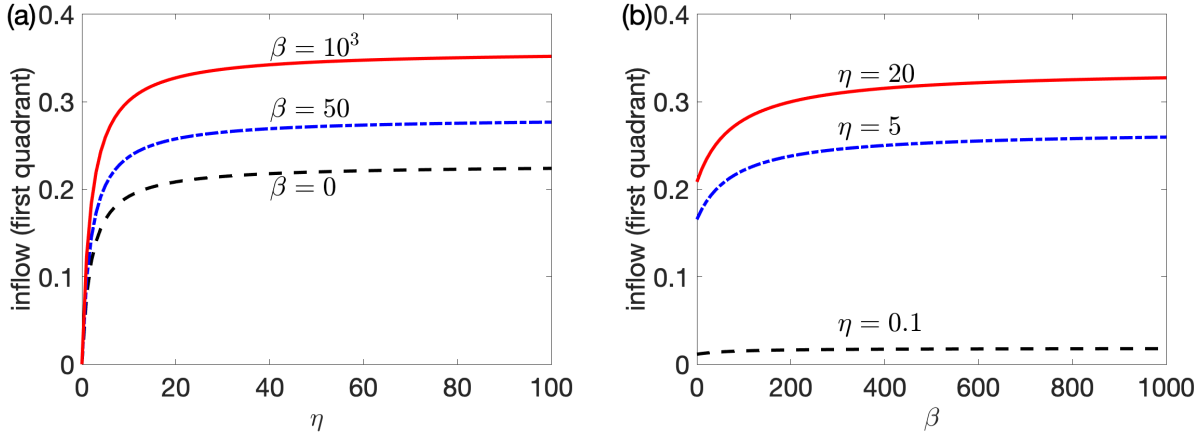

FIG. 4. Inflow into a poroelastic drop in a uniaxial extensional flow as a function of η (panel (a)) and β (panel (b)). $\Lambda = 1/3$, $\alpha_e = 0.005$ and $\phi_0 = 0.5$.

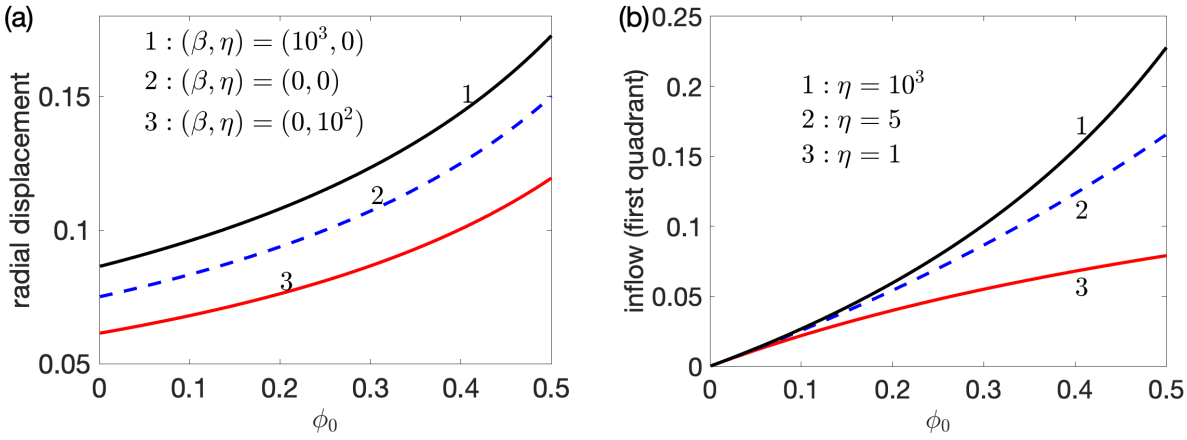

FIG. 5. Variation of radial displacement (panel (a)) and inflow (panel (b)) with respect to porosity ϕ_0. $\Lambda = 1/3$, and $\alpha_e = 0.005$. The interfacial slip $\beta = 0$ for results in panel (b).

inflow increases with both interfacial slip and permeability.

Figure 5 illustrates the effects of ϕ_0 on the radial displacement (panel (a)) and the inflow (panel (b)) at equilibrium. As $\phi_0 \to 0$ the drop interior becomes an elastic network (of large bending moduli) that deforms slightly in response to the exterior flow. When $\phi_0 \to 1$ the drop interior is nearly filled with fluid and will undergo very large deformation as there is no surface tension to resist deformation due to the exterior flow. As a result we focus on the range of $\phi_0 \in [0, 0.5]$ where the equilibrium radial displacement is in the small-deformation regime. Figure 5(b) shows the ϕ_0-variation of inflow for three values of η with $\beta = 0$. Consistent with results in figure 4, we observe that the inflow increases significantly with η from curve 3 ($\eta = 1$) to curve 2 ($\eta = 5$), and eventually plateaus to curve 1 for very large value of η. Similar behavior with η is observed for non-zero β.

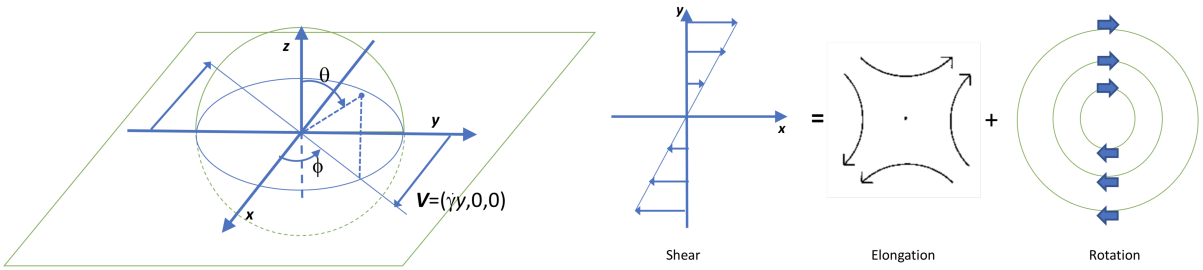

FIG. 6. *Left*: Illustration of a poroelastic drop in a planar shear flow $\mathbf{V} = (\dot{\gamma}y, 0, 0)$. *Right*: Decomposition of a planar shear flow into a straining component and a rotational component.

C. Planar shear flow

Figure 6 is an illustration of a drop in a planar shear flow with polar angle θ and azimuthal angle ϕ defined as labeled. A planar shear flow consists of a straining (compression and elongation) and a (rigid body) rotation. For a poroelastic drop in a planar shear flow the interior equilibrium solution takes the form

$$\widehat{p} = \frac{1}{2} d_1 r^2 \sin^2\theta \sin(2\phi), \tag{61}$$

$$\widehat{\mathbf{u}}_s \cdot \hat{\mathbf{r}} = \left(\frac{1}{7(1-\Lambda)(1-\phi_0)} d_1 r^3 + d_3 r + \frac{2\Lambda}{7+3\Lambda} d_4 r^3 \right) \sin^2\theta \sin(2\phi), \tag{62}$$

$$\widehat{\mathbf{u}}_s \cdot \hat{\theta} = \left(\frac{5}{21(1-\Lambda)(1-\phi_0)} d_1 r^3 + d_3 r + \frac{1}{3} d_4 r^3 \right) \sin\theta \cos\theta \sin(2\phi), \tag{63}$$

$$\widehat{\mathbf{u}}_s \cdot \hat{\phi} = \left(-\frac{r}{2} t + \left(\frac{5}{21(1-\Lambda)(1-\phi_0)} d_1 r^3 + d_3 r + \frac{1}{3} d_4 r^3 \right) \cos(2\phi) \right) \sin\theta. \tag{64}$$

$\hat{\mathbf{r}}$, $\hat{\theta}$ and $\hat{\phi}$ are the unit vectors in the r, θ, and ϕ directions, respectively. Note that now Equation (64) has a linear term $\frac{-r}{2}t$. This linear term represents a rotation of the deformable elastic network induced by the external planar shear flow under the small-deformation framework. Within the small-deformation framework, such linear temporal variation of $\widehat{\mathbf{u}}_s \cdot \hat{\phi}$ should be understood as a rotation along $\hat{\phi}$ on the unperturbed shape (a unit sphere.) The corresponding network rotation velocity at equilibrium is $\widehat{\mathbf{v}}_s = -r/2 \sin\theta \hat{\phi}$, which is a rigid body rotation and does not cause any viscous dissipation. Such rotation is also present in a viscous drop under a planar shear flow. We note that in the steady equilibrium solution ($\widehat{p}$ and $\widehat{\mathbf{u}}_s$ in the above equations) the components with a d_i dependence contribute to the elastic stress that is in balance with the pressure gradient.

The general solution for the exterior Stokes flow takes the form

$$\widehat{\mathbf{V}} \cdot \hat{\mathbf{r}} = \frac{1}{20r^4}\left(6C_3 + 5C_1 r^2 + 10r^5\right)\sin^2\theta \sin(2\phi), \tag{65}$$

$$\widehat{\mathbf{V}} \cdot \hat{\theta} = \frac{1}{20r^4}\left(-2C_3 + 5r^5\right)\sin(2\theta)\sin(2\phi), \tag{66}$$

$$\widehat{\mathbf{V}} \cdot \hat{\phi} = -\frac{1}{10r^4}\left(5(2C_4 r^2 + r^5) + (2C_3 - 5r^5)\cos(2\phi)\right)\sin\theta, \tag{67}$$

$$\widehat{P} = \frac{\alpha_e}{2r^3} C_1 \sin^2\theta \sin(2\phi). \tag{68}$$

The coefficient C_4 is zero, as expected from the small deformation analysis of a viscous drop in a planar shear flow. Altogether there are five coefficients $(d_1, d_3, d_4, C_1, C_3)$ to be determined from seven boundary conditions (Equations (44)-(48) in three dimensions), from which there are only five linearly independent equations (similar to the small-deformation analysis of a viscous drop). The coefficients are listed in Appendix C.

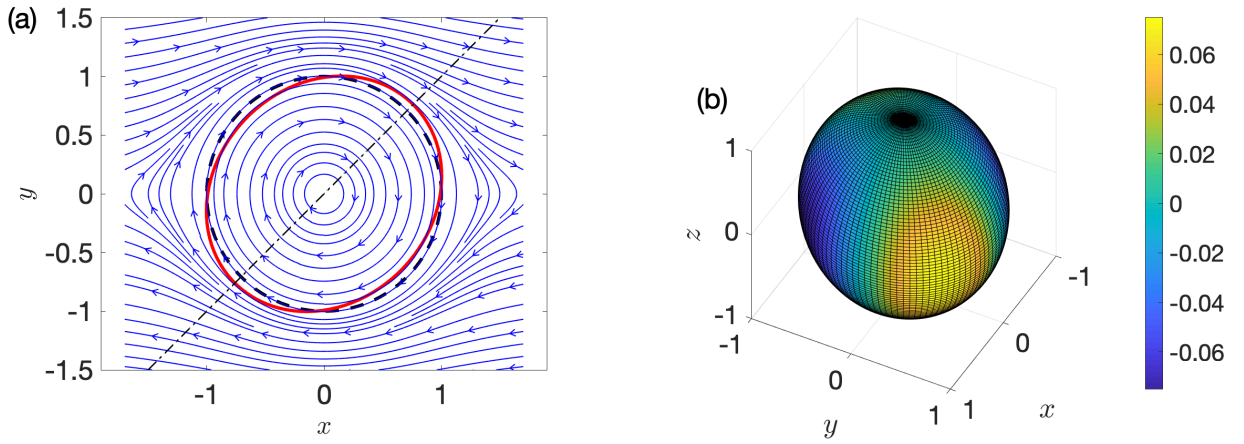

FIG. 7. Flow around a slightly deformable poroelastic drop under a simple shear flow with $\phi_0 = 0.5$, $\Lambda = 1/3$, $\alpha_e = 0.01$ and $(\beta, \eta) = (0, 0)$. (a): Cross section on the $x - y$ plane where the shear flow lies. Dashed curve is the initial spherical drop shape, and thick curve is the equilibrium deformation. The diagonal dash-dotted curve is the elongation axis in the shear flow (see figure (6)). (b): Three-dimensional rendition of $\hat{\mathbf{u}}_s \cdot \hat{\mathbf{r}}$. The color bar represents the magnitude of the radial displacement.

Figure (7)(a) visualizes the flow around a poroelastic drop under a shear flow with no interfacial slip $\beta = 0$ and interfacial permeability $\eta = 0$. In this case the displacement field is independent of the z-coordinate and we illustrate the flow and deformation on the $x - y$ plane. As in § III B, the small-deformation velocity field satisfies the boundary conditions on the unperturbed spherical drop surface. For $\beta = 0$ and $\eta = 0$, we expect the streamlines to circle around the unperturbed spherical drop (thick dashed curve in figure (7)(a)). The thick solid curve is the $x - y$ cross section of the equilibrium drop shape. The thin dash-dotted line is the elongation axis of a simple shear flow (see figure (6)).

In comparison with the flow around/in a viscous drop under a simple shear flow shown in figure (15) of Appendix A, we observe that the rotation of the network enhances the

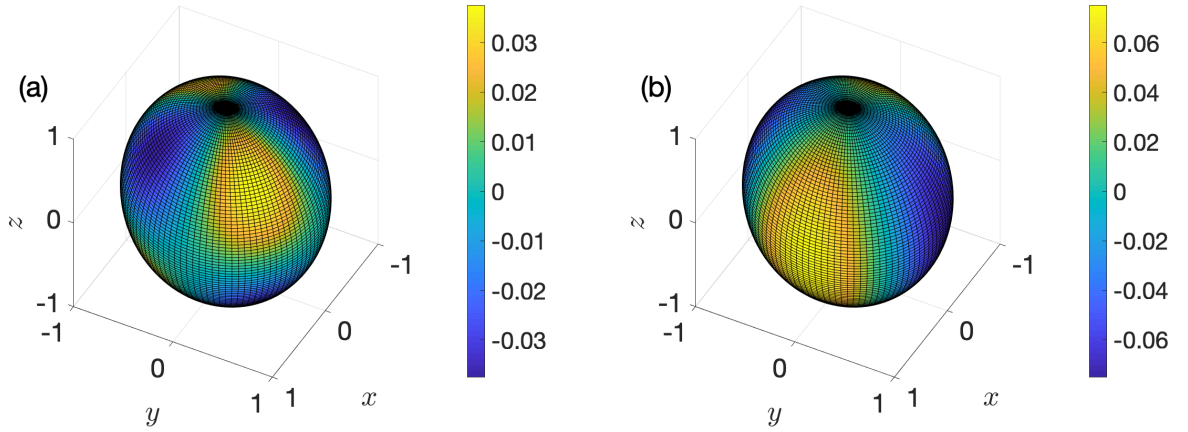

FIG. 8. Flow around a slightly deformable poroelastic drop under a simple shear flow with $\phi_0 = 0.5$, $\Lambda = 1/3$, $\alpha_e = 0.01$ and $(\beta, \eta) = (0, 0)$. (a): Three-dimensional rendition of $\hat{\mathbf{u}}_s \cdot \hat{\theta}$. (b): Three-dimensional rendition of $\hat{\mathbf{u}}_s \cdot \hat{\phi}$. The color bar represents the magnitude of the displacement.

vorticity inside a poroelastic drop, and the interior flow is more similar to a viscous drop with high interior viscosity. Figure (7)(b) is the contour plot of the radial displacement on the deformed poroelastic drop, and the color bar is for the magnitude of the radial displacement. Figure (8) shows the other two components of the displacement field (θ component in panel (a) and ϕ component in panel (b)). Note that for the ϕ component we only plot the time-independent component of the displacement. We observe that both $\hat{\mathbf{u}}_s \cdot \hat{\mathbf{r}}$ and $\hat{\mathbf{u}}_s \cdot \hat{\theta}$ reach maxima along the elongation axis.

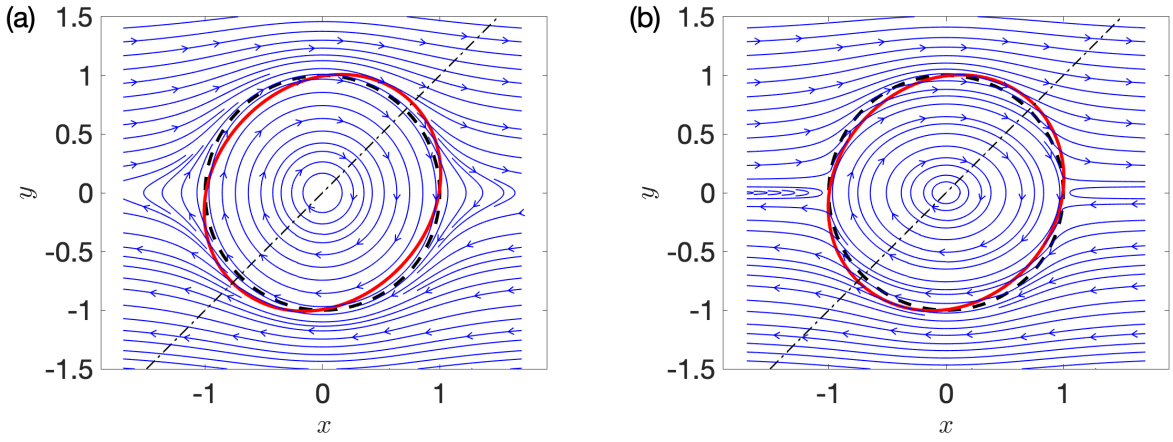

FIG. 9. Illustration of a slightly deformed poroelastic drop under a uniaxial extensional flow. Thin dashed line is the original spherical drop shape. Thick solid line is the equilibrium drop shape. Arrows between the two shapes indicate the equilibrium displacement field $\hat{\mathbf{u}}_s$ evaluated at $r = 1$. (a): $(\beta, \eta) = (10^2, 0)$. (b): $(\beta, \eta) = (10^3, 10)$.

As we increase the interfacial slip from $\beta = 0$ in figure 7 to $\beta = 10^2$ with $\eta = 0$, we find no significant difference in the flow pattern in figure (9)(a). However, a different flow

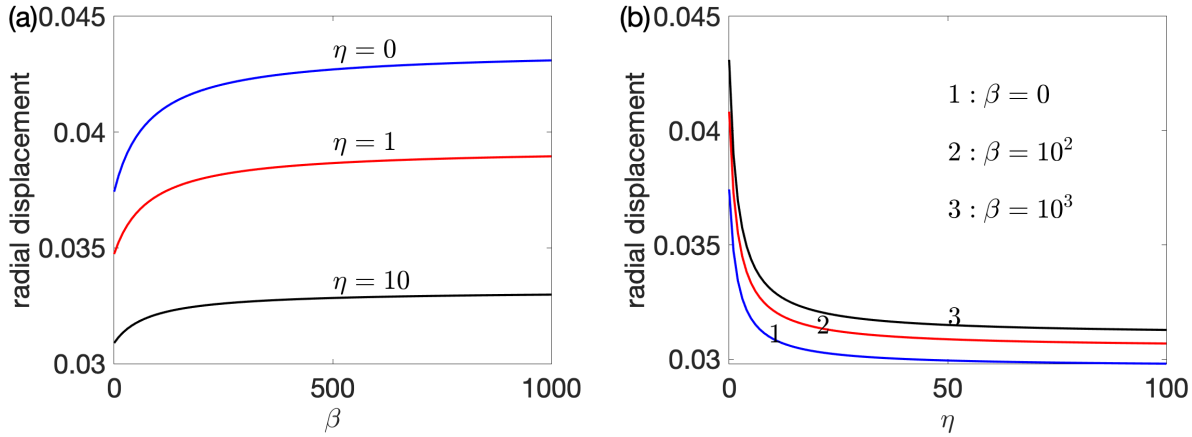

FIG. 10. Radial displacement $(\widehat{\mathbf{u}}_s \cdot \hat{\mathbf{r}})$ evaluated at $r = 1$ with $\Lambda = 1/3$, $\alpha_e = 0.005$ and $\phi_0 = 0.5$. (a) radial displacement versus β for three values of η as labeled. (b) radial displacement versus η for three values of β as labeled.

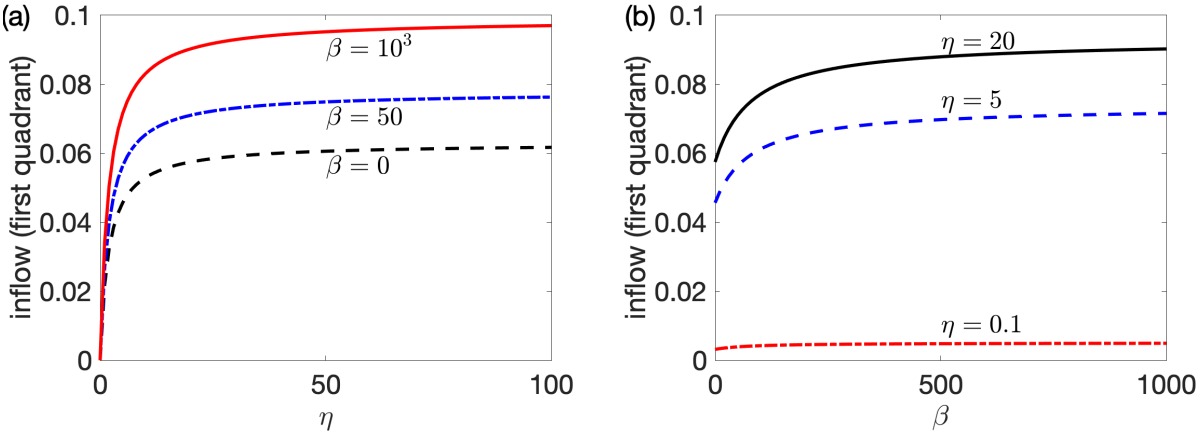

FIG. 11. Inflow into the first quarter of a poroelastic drop in a planar shear flow plotted against interfacial permeability η (panel (a)) and interfacial slip β (panel (b)). $\Lambda = 1/3$, $\phi_0 = 0.5$, and $\alpha_e = 0.005$.

pattern is observed when the interfacial permeability is increased to $\eta = 10$ in panel (b). When the interfacial permeability $\eta \neq 0$ fluid flow (streamlines) can go through the drop (the unperturbed shape denoted by thick dashed curves in figure (9)(b)). As a result of the permeating fluid flow the vorticity inside the drop takes an ellipsoidal shape. In addition, we observe a recirculation zone around the x-axis separating the up-streaming flow from down-streaming flow.

Figure 10 shows the radial displacement evaluated at the unperturbed drop surface ($r = 1$) as a function of interfacial slip (panel (a)) or interfacial permeability (panel (b)) with $\phi_0 = 0.5$, $\Lambda = 1/3$ and $\alpha_e = 0.005$. As in the previous extensional flow case, the displacement asymptotes to a constant value with increasing β and decreases with increasing η. Figure (11) shows the inflow in the first quadrant defined in Equation (60) for the planar shear flow case.

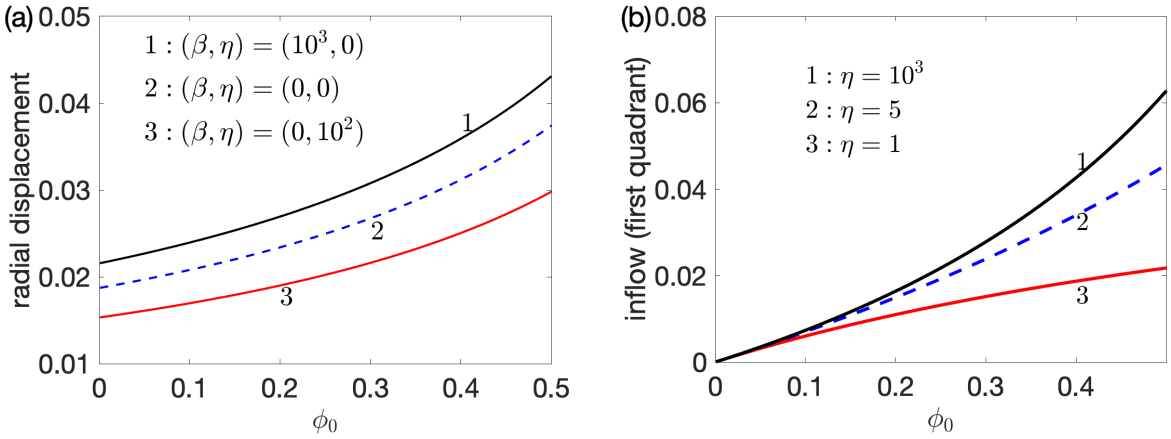

FIG. 12. Variation of radial displacement (panel (a)) and inflow (panel (b)) with respect to porosity ϕ_0. $\Lambda = 1/3$, and $\alpha_e = 0.005$. The interfacial slip $\beta = 0$ for results in panel (b).

We observe that the net inflow increases with both slip and permeability, similar to the case of uniaxial extensional flow. For the same values of the dimensionless parameters (α_e, Λ, β and η) the extension flow gives rise to larger inflow than the simple shear flow.

Figure 12 illustrates the effects of ϕ_0 on the equilibrium radial displacement (panel (a)) and the inflow (panel (b)) for a poroelastic drop in a simple shear flow. Comparing with results for the extension flow, we find that the radial displacement magnitude is smaller for the simple shear flow case with a similar trend in their dependence on both β and η.

D. Linear Dynamics

Similar to the case of a slightly deformable viscous drop in linear flows, the steady equilibrium solution for a slightly deformed poroelastic drop is obtained from solving a non-homogeneous equation. For a viscous drop in linear flows, the kinematic boundary condition gives rise to a first-order differential equation for the deformation amplitude that decays exponentially to the steady equilibrium. There is only one decay rate for a viscous drop, and it depends only on the viscosity ratio between internal and external viscous fluids. This is not the case for a poroelastic drop where the kinematic boundary condition is not sufficient for determining the linear dynamics characterized by a linear growth rate ω. Instead the homogeneous component of the general solution in Equation (54) produces a nonlinear eigenvalue problem for ω.

The time dependent linear solutions for a poroelastic drop in a uniaxial extensional flow and a planar shear flow are given in Appendix D and Appendix E, respectively. The two functions g_1 and g_2 satisfy differential equations with variable coefficients. See Supplemental Material at [URL will be inserted by publisher] [64] for these differential equations. Assuming Frobenius series, we obtain the following series solutions for g_1 and g_2 with coefficients that

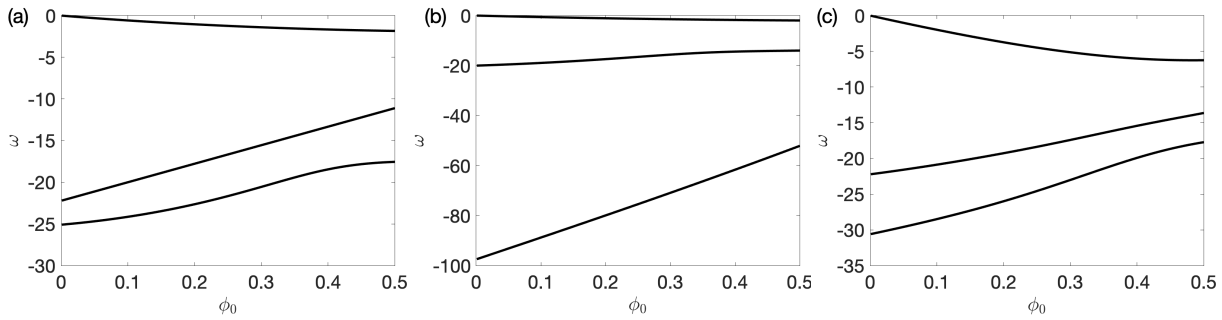

FIG. 13. Eigenvalue ω as a function of ϕ_0 with $\Lambda = 1/3$ and $\alpha_e = 10^{-2}$. (a) $(\beta, \eta) = (0, 0)$, (b) $(\beta, \eta) = (10^2, 0)$, and (c) $(\beta, \eta) = (0, 10)$.

depend on the eigenvalue ω:

$$g_1(r) = r^5 + \frac{2\bar{\omega}}{99} r^7 + \frac{5\bar{\omega}^2}{20592} r^9 + \frac{\bar{\omega}^3}{514800} r^{11} + \cdots , \tag{69}$$

$$g_2(r) = \frac{28}{\bar{\omega}} r^3 - \frac{1}{3} r^5 - \frac{\bar{\omega}}{198} r^7 - \frac{\bar{\omega}^2}{20592} r^9 - \frac{\bar{\omega}^3}{3088800} r^{11} + \cdots , \tag{70}$$

where $\bar{\omega} \equiv \omega/\phi_0$. For the uniaxial extensional flow case, the coefficients (a_1, a_2) in Equations (D6)-(D7) can be expressed in terms of $(\alpha_1, \alpha_3, \alpha_5)$. For the planar shear flow case, the coefficients (c_1, c_3) in Equations (E8)-(E11) can be eliminated as well. For both uniaxial and shear flow, the the resultant system of linear equations for $(\alpha_1, \alpha_3, \alpha_5)$ are thus a nonlinear eigenvalue problem for ω:

$$\mathbf{A} \begin{pmatrix} \alpha_1 \\ \alpha_3 \\ \alpha_5 \end{pmatrix} = \omega \mathbf{B}(\omega) \begin{pmatrix} \alpha_1 \\ \alpha_3 \\ \alpha_5 \end{pmatrix} . \tag{71}$$

Solutions of Equation (71) for ω describe the linear dynamics of a poroelastic drop in the small-deformation limit. Identical matrixes $\mathbf{A}$ and $\mathbf{B}$ are obtained for both the uniaxial extensional flow and the planar shear flow: This is consistent with the small-deformation dynamics of a viscous drop in linear flows. This means that the same eigenvalues are expected for both the uniaxial extensional flow and the planar shear flow. See Supplemental Material at [URL will be inserted by publisher] [64] for the characteristic equations in matrix form.

Figures (13) show the first three eigenvalues from solving the nonlinear eigenvalue problem in Equation (71) for three cases with different combination of β and η. For all these results, sufficient terms in the power series for g_1 and g_2 are used to guarantee convergence in finding the eigenvalue ω. For all three combinations of (β, η), we calculate the eigenvalues for $\phi_0 \in (0, 0.5)$ where the small deformation assumption is valid. Our computation also shows that all eigenvalues of Equation (71) are negative, implying that the steady equilibrium solutions that we found are stable. This is similar to the case of a slightly deformable viscous drop stabilized by a strong surface tension.

IV. CONCLUSIONS AND ONGOING RESEARCH

In this work we develop a two-phase flow model for a poroelastic fluid that consists of an elastic network fully immersed in a viscous fluid. This model is equivalent to the incompressible Brinkmann equations when the network is rigid and does not move in the reference frame. If the viscous dissipation in the poroelastic fluid is sub-dominated by the pressure gradient force and the friction force, our two-phase flow model is reduced to Darcy flow with a deformable network phase. Appropriate boundary conditions at the boundary between the biphasic poroelastic fluid and a viscous Stokes flow are derived by the free energy dissipation principle.

Applying this model to the small-deformation dynamics of a poroelastic drop under linear flows, we are able to find steady equilibrium solutions and examine the effects of interfacial slip and permeability on the radial displacement and the flow around the drop. Under a uniaxial extensional flow, non-zero interfacial permeability gives rise to an interior flow, coming into the drop along the compression axis and leaving the drop along the extension axis. Under a planar shear flow, the network rotates with the vorticity in the shear flow. Such a rigid-body rotation is the dominant interior flow at a steady equilibrium in the absence of permeability. Different flow patterns develop around the drop more due to the interfacial slip than permeability. In general we find that the radial displacement decreases with increasing interfacial permeability, while interfacial slip enhances the radial displacement.

The kinematic boundary condition for a poroelastic drop governs the interface moving with the normal component of the network velocity at the interface. This renders the eigenvalue problem nonlinear and we are able to compute the first three eigenvalues. We find that the eigenvalues are the same for both extensional and shear flow, and all the eigenvalues are real and negative. These are similar to the small-deformation dynamics of a viscous drop in linear flows.

In the small-deformation limit we assume that the unperturbed volume fraction for the fluid phase is homogeneous. This simplification avoids the complication of having to solve a linear system of variable-coefficient boundary value equations. In addition this simplification greatly reduces the porosity dependence on the volume fraction. Based on results from MacMinn *et al.* [47] a nonhomogeneous initial volume fraction and a more complicated porosity may not alter the linear dynamics and steady equilibria significantly.

Although our two-phase flow model does not capture the complexity of many biological poroelastic fluids of interest, one expectation is that this approach can be generalized to consider more complex situations such as the swelling and drying due to chemical reaction, polyelectrolytic properties of the solvents in gel-like solutions, and the nonlinear elastohydrodynamics when the displacement amplitude is large. These are all promising directions that we plan to apply our model to after we validate our small-deformation results by comparing against direct numerical simulation results. Currently we are conducting the small-deformation analysis on a soft Brinkman drop (that may be more appropriate for low volume fraction $\phi_s < 5\%$, see the derivations in Caflisch and Rubinstein [1]) in linear flows.

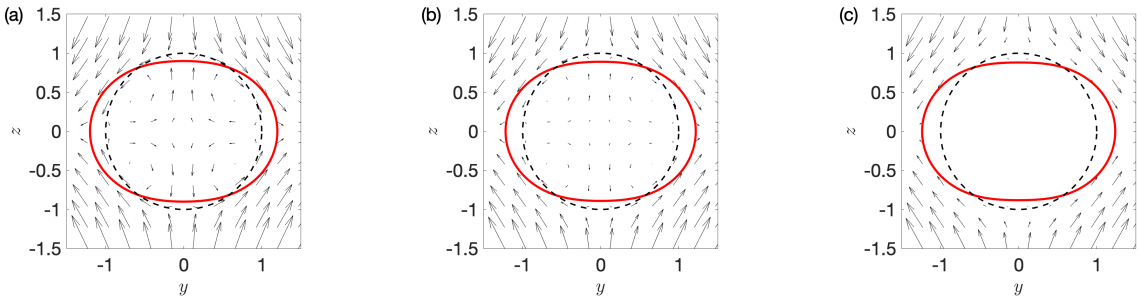

FIG. 14. Cross section ($x = 0$ plane) of a viscous drop in a uniaxial extension flow. The dashed curve is the original spherical shape, and the thick curve is the equilibrium drop shape with $Ca = 0.1$. The viscosity ratio (interior to exterior) is 10^{-2}, 1 and 10^3 from left to right.

ACKNOWLEDGMENTS

YNY would like to acknowledge helpful discussions with M. Shelley. The authors acknowledge support from NSF-DMS 1614863 and 1412789 (YNY), NSF-DMS 1516978 and 1620316 (YM) and NSF-DMS 1716144 (MJM).

Appendix A: A viscous drop in linear flow

For comparison here we show the equilibrium solution of a viscous drop in both a uniaxial extension flow and a simple shear flow. The strong surface tension (small capillary number $Ca \ll 1$) balances the viscous stress under a fluid flow. The equilibrium small-deformation solutions are available in the literature and here we used the equilibrium solution from [42] for the following figures.

Under a uniaxial extension flow $\mathbf{U}_\infty = E(x, y, -2z)$, the small-deformation solution is symmetric around the z axis and we show the equilibrium drop shape and flow in the $y - z$ plane in figure (14). The interior flow pattern consists a pair of dipole vortices of strength that decreases with the increasing viscosity ratio.

For a viscous drop under a simple shear flow $\mathbf{U}_\infty = \dot{\gamma}(y, 0, 0)$ the drop shape depends on both θ and ϕ. Here we show the small-deformation solution in the $z = 0$ plane in figure (15). We observe that the strength of flow around the $y = 0$ axis increases as the interior fluid viscosity increases.

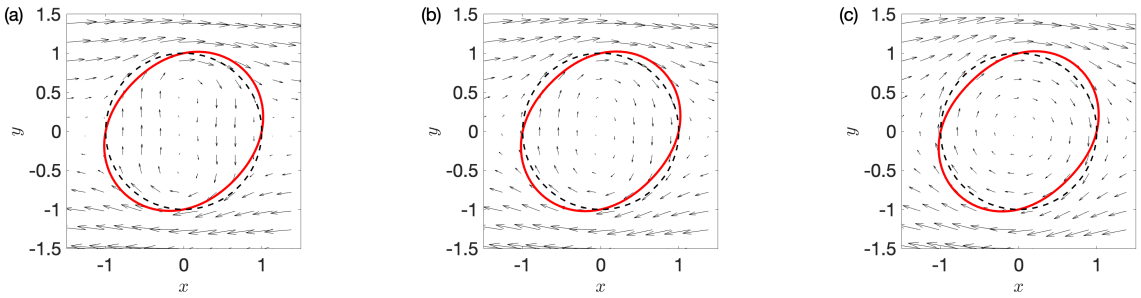

FIG. 15. Cross section ($z = 0$ plane) of a viscous drop in a simple shear flow. The dashed curve is the original spherical shape, and the thick curve is the equilibrium drop shape with $Ca = 0.1$. The viscosity ratio (interior to exterior) is 10^{-2}, 1 and 10^3 from left to right.

Appendix B: Steady Equilibrium under a Uniaxial Extensional Flow

For a poroelastic drop at the steady equilibrium under a uniaxial extensional flow, the coefficients are

$$d_1 = -\frac{50(4\beta+1)\eta}{7(1-\Lambda)(5\beta\eta\phi_0 - 5\beta\eta - 48\beta\eta\phi_0 - 10\beta\phi_0 + 2\eta\phi_0 - 2\eta - 24\eta\phi_0 - 4\phi_0)}, \tag{B1}$$

$$d_2 = \frac{N_{d_2}}{D_{d_2}}, \tag{B2}$$

$$\begin{aligned} N_{d_2} =& 15(40\beta\eta\Lambda\phi_0 - 40\beta\eta\Lambda + 24\beta\eta\phi_0 - 24\beta\eta - 72\beta\Lambda\phi_0 - 56\beta\phi_0 + \\ & 13\eta\Lambda\phi_0 - 13\eta\Lambda - 48\eta\Lambda\phi_0 + 6\eta\phi_0 - 6\eta - 24\Lambda\phi_0 - 14\phi_0), \\ D_{d_2} =& (1-\Lambda)(12\Lambda+7)(\phi_0-1)(5\beta\eta\phi_0 - 5\beta\eta - 48\beta\eta\phi_0 - 10\beta\phi_0 + \\ & 2\eta\phi_0 - 2\eta - 24\eta\phi_0 - 4\phi_0), \end{aligned}$$

$$d_3 = \frac{N_{d_3}}{D_{d_3}}, \tag{B3}$$

$$\begin{aligned} N_{d_3} =& 9(3\Lambda+7)(-32\beta\eta\Lambda\phi_0 + 32\beta\eta\Lambda - 32\beta\eta\phi_0 + 32\beta\eta + 280\beta\phi_0 - \\ & 8\eta\Lambda\phi_0 + 8\eta\Lambda + 27\eta\phi_0 - 27\eta - 560\eta\phi_0), \\ D_{d_3} =& 7D_{d_2}, \end{aligned}$$

$$A_1 = \frac{10(\beta\eta\phi_0 - \beta\eta + 16\beta\eta\phi_0 - 2\beta\phi_0 + \eta\phi_0 - \eta - 8\eta\phi_0 - 2\phi_0)}{5\beta\eta\phi_0 - 5\beta\eta - 48\beta\eta\phi_0 - 10\beta\phi_0 + 2\eta\phi_0 - 2\eta - 24\eta\phi_0 - 4\phi_0}, \tag{B4}$$

$$A_2 = -\frac{6(16\beta\eta\phi_0 + \eta\phi_0 - \eta - 12\eta\phi_0 - 2\phi_0)}{5\beta\eta\phi_0 - 5\beta\eta - 48\beta\eta\phi_0 - 10\beta\phi_0 + 2\eta\phi_0 - 2\eta - 24\eta\phi_0 - 4\phi_0}. \tag{B5}$$

Appendix C: Steady Equilibrium under a Planar Shear Flow

For a poroelastic drop at the steady equilibrium under a planar shear flow, the coefficients are

$$C_1 = -\frac{10(\beta\eta(\phi_0-1)+16\beta\eta\phi_0-2\phi_0(\beta+4\eta)+\eta(\phi_0-1)-2\phi_0)}{5\beta\eta(\phi_0-1)-48\beta\eta\phi_0-2\phi_0(5\beta+12\eta)+2\eta(\phi_0-1)-4\phi_0}, \tag{C1}$$

$$C_3 = \frac{5(16\beta\eta\phi_0+\eta(\phi_0-1)-12\eta\phi_0-2\phi_0)}{5\beta\eta(\phi_0-1)-48\beta\eta\phi_0-2\phi_0(5\beta+12\eta)+2\eta(\phi_0-1)-4\phi_0}, \tag{C2}$$

$$d_1 = \frac{10(4\beta+1)\eta(\phi_0-1)}{-5\beta\eta(\phi_0-1)+48\beta\eta\phi_0+2\phi_0(5\beta+12\eta)-2\eta(\phi_0-1)+4\phi_0}, \tag{C3}$$

$$d_3 = \frac{N_{d_3}}{D_{d_3}}, \tag{C4}$$

$$\begin{aligned} N_{d_3} =& -5(2(20\beta\eta\Lambda(\phi_0-1)+12\beta\eta(\phi_0-1)-12\Lambda\phi_0-7\phi_0)- \\ & 8\phi_0(9\beta\Lambda+7\beta+6\eta\Lambda)+\eta(13\Lambda+6)(\phi_0-1)), \\ D_{d_3} =& (1-\Lambda)(12\Lambda+7)(\phi_0-1)(5\beta\eta(\phi_0-1)-48\beta\eta\phi_0-2\phi_0(5\beta+12\eta)+2\eta(\phi_0-1)-4\phi_0), \end{aligned}$$

$$d_4 = \frac{3(3\Lambda+7)(32\beta\eta(\Lambda+1)(\phi_0-1)-280\phi_0(\beta-2\eta)-\eta(27-8\Lambda)(\phi_0-1))}{7D_{d_3}}. \tag{C5}$$

Appendix D: Linear solutions under a Uniaxial Extensional Flow

The displacement field is given by

$$\mathbf{u}_{s,1}\cdot\hat{\mathbf{r}} = \frac{h_0(r)}{3}\left(1+3\cos(2\theta)\right)e^{\omega t}, \tag{D1}$$

$$\mathbf{u}_{s,1}\cdot\hat{\theta} = h_1(r)\sin(2\theta)e^{\omega t}, \tag{D2}$$

and the flow field is given by

$$\begin{aligned} p_1 =& \frac{(1-\phi_0)}{12r}\left[(8(1+\omega\mu_s)h_0+2(1+\Lambda+\omega\mu_s)rh_0'\right)+ \\ & \left(12(1+\omega\mu_s)h_1-2(1-\Lambda+\omega\mu_s)rh_1'-2(1-\Lambda+\omega\mu_s)r^2h_1''\right)\left(1+3\cos(2\theta)\right)e^{\omega t}, \end{aligned} \tag{D3}$$

$$h_0 = \alpha_1 r+\alpha_3 r^3+\alpha_5 g_1(r), \tag{D4}$$

$$h_1 = -\alpha_1 r-\frac{5}{3}\alpha_3 r^3+\alpha_5 g_2(r), \tag{D5}$$

$$\psi_{e,1} = \left(\frac{a_1}{2}-\frac{a_2}{2r^2}\right)\cos\theta\sin^2\theta e^{\omega t}, \tag{D6}$$

$$P_1 = -\frac{\alpha_e}{2r^3}a_1\left(1+3\cos(2\theta)\right)e^{\omega t}. \tag{D7}$$

Appendix E: Linear solutions under a Planar Shear Flow

The displacement field is given by

$$\mathbf{u}_{s,1} \cdot \hat{\mathbf{r}} = f_0(r) \sin^2\theta \sin(2\phi) e^{\omega t}, \tag{E1}$$

$$\mathbf{u}_{s,1} \cdot \hat{\theta} = \frac{f_1(r)}{2} \cos(2\theta) \sin(2\phi) e^{\omega t}, \tag{E2}$$

$$\mathbf{u}_{s,1} \cdot \hat{\phi} = f_1(r) \sin\theta \cos(2\phi) e^{\omega t}, \tag{E3}$$

$$\tag{E4}$$

and the flow field is given by

$$p_1 = \frac{(1-\phi_0)}{4r} \left[(8(1+\omega\mu_s) f_0 + 2(1+\Lambda+\omega\mu_s) r f_0') - \right. \tag{E5}$$
$$\left. \left(12(1+\omega\mu_s) f_1 - 2(1-\Lambda+\omega\mu_s) r f_1' - 2(1-\Lambda+\omega\mu_s) r^2 f_1'' \right) \right] (1+3\cos(2\theta))\, e^{\omega t},$$

$$f_0 = \alpha_1 r + \alpha_3 r^3 + \alpha_5 g_1(r), \tag{E6}$$

$$f_1 = \alpha_1 r + \frac{5}{3}\alpha_3 r^3 - \alpha_5 g_2(r), \tag{E7}$$

$$\mathbf{V}_1 \cdot \hat{\mathbf{r}} = \frac{1}{20 r^4} \left(c_3 + 5 c_1 r^2 \right) \sin^2\theta \sin(2\phi) e^{\omega t}, \tag{E8}$$

$$\mathbf{V}_1 \cdot \hat{\theta} = -\frac{1}{10 r^4} c_3 \sin(2\theta) \sin(2\phi) e^{\omega t}, \tag{E9}$$

$$\mathbf{V}_1 \cdot \hat{\phi} = -\frac{1}{10 r^4} \left(10 c_4 r^2 + 2 c_3 \cos(2\phi) \right) \sin\theta e^{\omega t}, \tag{E10}$$

$$P_1 = \frac{\alpha_e}{2 r^3} c_1 \sin^2\theta \sin(2\phi) e^{\omega t}. \tag{E11}$$

---

[1] R. E. Caflisch and J. Rubinstein, "Chapter 6: Flow in porous media," in *Lectures on the mathematical theory of multi-phase flow* (New York University, 1986).

[2] J. M. Carcione, "Chapter 7: Biot's theory for porous media," in *Handbook of geophysical exploration: seismic exploration*, edited by K. Helbig and S. Treitel (Pergamon, 2001).

[3] W. M. Lai, J. S. Hou, and V. C. Mow, "A triphasic theory for the swelling and deformation behaviors of articular cartilage," J. Biomech. Eng. **113**, 245–258 (1991).

[4] P. M. Pinsky, "Three-dimensional modeling of metabolic species transport in the cornea with a hydrogel intrastromal inlay," Invest Ophthalmol Vis. Sci. **55**, 3093–3106 (2014).

[5] X. Chen, S. J. Petsche, and P. M. Pinsky, "A structural model for the in vivo human cornea including collagen-swelling interaction," J. R. Soc. Interface **12**, 20150241 (2015).

[6] P. M. Pinsky and X. Cheng, "A constitutive model for swelling pressure and volumetric behavior of highly-hydrated connective tissue," J. Elast. **129**, 145–170 (2017).

[7] N. G. Cogan and J. P. Keener, "The role of the biofilm matrix in structural development," Math. Med. Biol. **21**, 147–166 (2004).

[8] Y. Mori, H. Chen, C. Micek, and M.-C. Calderer, "A dynamic model of polyelectrolyte gels," SIAM J. Appl. Math. **73**, 103–133 (2013).

[9] W. Strychalski, C. A. Copos, O. L. Lewis, and R. D. Guy, "A poroelastic immersed boundary method with applications to cell biology," J. Comp. Phys. **282**, 77–97 (2015).

[10] W. Strychalski and R. D. Guy, "Intracellular pressure dynamics in blebbing cells," Biophys. J. **110**, 1168–1179 (2016).

[11] D. A. Drew, "Mathematical modeling of two-phase flow," Ann. Rev. Fluid Mech. **15**, 261–291 (1983).

[12] R. Burridge and J. B. Keller, "Poroelasticity equations derived from microstructures," J. Acoustical Society of America **70**, 1140 (1981).

[13] E. Holland and R. E. Showalter, "Poro-visco-elastic compaction in sedimentary basins," SIAM J. Math. Anal. **50**, 2295–2316 (2018).

[14] F. A. Morales and R. E. Showalter, "A Darcy-Brinkman model of fractures in porous media," J. Math. Anal. Appl. **452**, 1332–1358 (2017).

[15] L. Bociu, G. Guidoboni, R. Sacco, and J. T. Webster, "Analysis of nonlinear poro-elastic and poro-visco-elastic models," Arch. Rational Mech. Anal. **222**, 1445–1519 (2016).

[16] H. T. Banks, K. Bekele-Maxwell, L. Bociu, M. Noorman, and G. Guidoboni, "Sensitivity analysis in poro-elastic and poro-visco-elastic models with respect to boundary data," Quaterly of Applied Mathematics **4**, 697–735 (2017).

[17] M. Verri, G. Guidoboni, L. Bociu, and R Sacco, "The role of structural viscoelasticity in deformable porous media with incompressible constituents: applications in biomechanics," Math. Biosci. Eng. **15**, 939–959 (2018).

[18] P. Angot, B. Goyeau, and J. A. Ochoa-Tapia, "Asymptotic modeling of transport phenomena at the interface between a fluid and a porous layer: Jump conditions," Phys. Rev. E **95**, 063302 (2017).

[19] P. Angot, G. Carbou, and V. Peron, "Asymptotic study for Stokes-Brinkman model with jump embedded transmission conditions," Asymptotic Analysis **96**, 223–249 (2016).

[20] P. Angot, "On the well-posed coupling between free fluid and porous viscous flows," Applied Math. Lett. **24**, 803–810 (2011).

[21] J. A. Ochoa-Tapia, "Momentum transfer at the boundary between a porous medium and a homogeneous fluid - ii. comparison with experiment," Int. J. Heat Mass Transfer **38**, 2647–2655 (1995).

[22] G. S. Beavers and D. D. Joseph, "Boundary conditions at a naturally permeable wall," J. Fluid Mech. **30**, 197–207 (1967).

[23] D. R. Hewitt, J. S. Nijjer, M. G. Worster, and Jerome A. Neufeld, "Flow-induced compaction of a deformable porous medium," Phys. Rev. E **93**, 023116 (2016).

[24] M. L. Bars and M. G. Worster, "Interfacial conditions between a pure fluid and a porous medium: implications for binary alloy solidification," J. Fluid Mech. **550**, 149–173 (2006).

[25] P. G. Saffman, "On the boundary condition at the surface of a porous medium," Studies Applied Math. **2**, 93–101 (1971).

[26] G. Neale and W. Nader, "Creeping flow relative to permeable spheres," Chem. Eng. Sci. **28**, 1865–1874 (1973).

[27] G. Neale and W. Nader, "Practical significance of Brinkman's extension of Darcy's law: coupled parallel flows within a channel and a bounding porous medium," Can. J. Chem. Eng. **52**,

475–478 (1974).

[28] I.-S. Liu, "On chemical potential and incompressible porous media," J. de Mecanique **19**, 327–342 (1980).

[29] S. Haber and R. Mauri, "Boundary conditions for Darcy's flow through porous media," Int. J. Multiphase Flow **9**, 561–574 (1983).

[30] A. F. Mak, "The apparent viscoelastic behavior of articular cartilage?the contributions from the intrinsic matrix viscoelasticity and interstitial fluid flows," J. Biomech. Eng. **108**, 123–130 (1986).

[31] V. C. Mow, M. H. Holmes, and W. M. Lai, "Fluid transport and mechanical properties of articular cartilage: a review," J. Biomech. **17**, 377–394 (1984).

[32] J. S. Hou, M. H. Holmes, W. M. Lai, and V. C. Mow, "Boundary conditions at the cartilage-synovial fluid interface for joint lubrication and theoretical verifications," J. Biomech. Eng. **111**, 78–87 (1989).

[33] E. I. Saad, "Stokes flow past an assemblage of axisymmetric porous spherical shell-in-cell models: effect of stress jump condition," Meccanica **48**, 1747–1759 (2013).

[34] E. I. Saad and M. S. Faltas, "Slow motion of a porous sphere translating along the axis of a circular cylindrical pore subject to a stress jump condition," Transp. Porous Med. **102**, 91–109 (2014).

[35] E. I. Saad, "Axisymmetric motion of a porous sphere through a spherical envelop subject to a stress jump condition," Meccanica **51**, 799–817 (2016).

[36] U. Lacis, G. A. Zampogna, and S. Bagheri, "A computational continuum model of poroelastic beds," Proc. R. Soc. A , 20160932 (2017).

[37] U. Lacis and S. Bagheri, "A framework for computing effective boundary conditions at the interface between fluid and a porous medium," J. Fluid Mech. **812**, 866–889 (2017).

[38] G. Dagan, "The generalization of Darcy's law for nonuniform flows," Water Resources Research **15**, 1–7 (1979).

[39] W. Jager and A. Mikelic, "Modeling effective interface laws for transport phenomena between an unconfined fluid and a porous medium using homogenization," Transp. Porous Med. **78**, 489–508 (2009).

[40] T. Carraro, C. Goll, A. Marciniak-Czochra, and A. Mikelic, "Pressure jump interface law for the Stokes-Darcy coupling: confirmation by direct numerical simulations," J. Fluid Mech. **732**, 510–536 (2013).

[41] H. A. Stone, "Dynamics of drop deformation and breakup in viscous fluids," Annu. Rev. Fluid Mech. **26**, 65–102 (1994).

[42] L. Gary Leal, "Chapter 8: Creeping flow - three-dimensional problems," in *Advanced Transport Phenomena* (Cambridge University Press, 2007).

[43] Seung-Man Yang and Won-Hi Hong, "Motions of a porous particle in stokes flow: part 1. unbounded single-fluid domain problem," Korean J. Chem. Eng. **5**, 23–34 (1988).

[44] Seung-Man Yang and Won-Hi Hong, "Motions of a porous particle in stokes flow: part 2. unbounded single-fluid domain problem," Korean J. Chem. Eng. **6**, 234–245 (1989).

[45] Seung-Man Yang and L. Gary Leal, "Motions of a porous particle in stokes flow near a plane-fluid interface," Physicochemical Hydrodynamics **11**, 543–569 (1989).

[46] R. H. Davis and H. A. Stone, "Flow through beds of porous particles," Chem. Eng. Sci. **48**, 3993–4005 (1993).

[47] C. W. MacMinn, E. R. Dufresne, and J. S. Wettlaufer, "Large deformation of a soft porous material," Phys. Rev. Applied **5**, 044020 (2016).

[48] C. A. Weber, C. H. Rycroft, and L. Mahadevan, "Differential activity-driven instabilities in biphasic active matter," Phys. Rev. Lett. **120**, 248003 (2018).

[49] S. S. Antman, in *Nonlinear problems of elasticity* (Springer, New York, 1995).

[50] M. E. Gurtin, E. Fried, and L. Anand, in *The mechanics and thermodynamics of continua* (Cambridge University Press, 2010).

[51] M. A.Haider, "A radial biphasic model for local cell-matrix mechanics in articular cartilage," SIAM J. Appl. Math. **64**, 1588–1608 (2004).

[52] L. G. Aleopoulos, G. M. Williams, M. L. Upton, L. A. Setton, and F. Guilak, "Osteoarthritic changes in the biphasic mechanical properties of the chondrocyte pericellular matrix in articular cartilage," J. Biomech. **38**, 509–517 (2005).

[53] H. T. Nia, I. S. Bozchalooi, Y. Li, L. Han, H.-H. Hung, E. Frank, K. Youcef-Toumi, C. Ortiz, and A. Grodzinsky, "High-bandwidth afm-based rheology reveals that cartilage is most sensitive to high loading rates at early stages of impairment," Biophys. J. **104**, 1529–1537 (2013).

[54] H. T. Nia, L. Han, I. S. Bozchalooi, P. Roughley, K. Youcef-Toumi, A. J. Grodzinsky, and C. Ortiz, "Aggrecan nanoscale solid-fluid interactions are a primary deterinant of cartilage dynamic mechanical properties," ACS Nano. **9**, 2614–2625 (2015).

[55] Y. Li, Y. Mori, and S. X. Sun, "Flow-driven cell migration under external electric fields," Phys. Rev. Lett. **115**, 268101 (2015).

[56] J. P. Rothstein, "Slip on superhydrophobic surfaces," Annu. Rev. Fluid Mech. **42**, 89–109 (2010).

[57] A. Maali and B. Bhushan, "Measurement of slip length on superhydrophobic surfaces," Phil. Trans. R. Soc. A **370**, 2304–2320 (2011).

[58] E. Lauga, M. P. Brenner, and H. A. Stone, "Microfluidics: The no-slip boundary condition," in *Handbook of Experimental Fluid Dynamics*, edited by C. Tropea, A. Yarin, and J. F. Foss (Springer, New York, 2007).

[59] H. J. Keh and Y. C. Chang, "Creeping motion of a slip spherical particle in a circular cylindrical pore," Int. J. Multiphase Flow **33**, 726–741 (2007).

[60] M. A. Haider and F. Guilak, "An axisymmetric boundary integral model for assessing elastic cell properties in micropipette aspiration test," J. Biomech. Engrg. **124**, 586–595 (2002).

[61] M. A. Haider an B. A. Benedict, E. Kim, and F. Guilak, "Chapter 11: Computational modeling of cell mechanics in articular cartilage," in *Computational Modeling in Biomechanics* (Springer Science+Business, 2010).

[62] A. Ramachandran, K. Tsigklifis, A. Roy, and G. Leal, "The effect of interfacial slip on the dynamics of a drop in flow: Part i. stretching, relaxation, and breakup," J. Rheol. **56**, 45 (2012).

[63] S. Das, S. Mandal, S. K. Som, and S. Chakraborty, "Effect of interfacial slip on the deformation of a viscoelastic drop in uniaxial extensional flow field," Phys. Fluids **29**, 032105

(2017).
[64] Supplementary material, see https://.